

SOIL-ORE PROCESSING OF CONTINUOUS
MULAYER FURNACE

By

SALMAN AL-ASSAMI

A DISSERTATION PRESENTED TO THE GRADUATE SCHOOL
OF THE UNIVERSITY OF FLORIDA, IN PARTIAL FULFILLMENT
OF THE REQUIREMENTS FOR THE DEGREE OF
DOCTOR OF PHILOSOPHY

UNIVERSITY OF FLORIDA

DEDICATION

I dedicate this dissertation to my parents.
Their love, support and wisdom have been and always
will be a constant source of strength and inspiration.

ACKNOWLEDGMENTS

I would like to take this opportunity to acknowledge the members of my dissertation committee. Dr. Joseph H. Simmons, chair of my committee, for the support and guidance he provided throughout the research and Drs. E.D. Whitney, A.B. Beutner and B.V. Barker for their enculturation and willingness to serve on my committee. I also wish to express special thanks to Dr. Michael Banks for his informative discussions on this project.

I would also like to thank Guy Lefebvre, Richard Crozier and Augusta Moenier for their assistance in characterizing samples. Special thanks to Terry Chen, John McHugh and all the members of Dr. Simmons' and Dr. Banks' groups. I would also like to thank Catherline Resources for her informative oppositions to this project. I also extend my appreciation to Roberta Schulte for her assistance in editing this manuscript.

Finally, I am deeply indebted to my father, mother, sister and brother. Without their love and support, this work would not have been possible.

TABLE OF CONTENTS

ACKNOWLEDGEMENTS	iii
ABSTRACT	iii
CHAPTERS	
1 INTRODUCTION	1
Statement of Problem	2
Objectives	2
2 LITERATURE SURVEY	3
Molten Processing Via Sol-Gel	3
Definite Gels	3
Single Phase Gels	12
Continuous Molten Phase Gels	12
Sol-Gel Processing	16
Commercially Available Molten Fibers	17
3 SOL-GEL PROCESSING	19
Introduction	21
Stability of Colloidal Sol	21
Surface Energy	21
Van der Waals Forces	23
Electrostatic Repulsion	23
The Structure of The Electro Double Layer	24
Polymer Stabilization	27
Sol-Gel Processing Agents	29
Hydrolysis and Polycondensation	29
Hydrolysis and Crosslinking of Inorganic Precursors	30
Hydrolysis and Polycondensation of Metal Alkoxides	41
Metal Alkoxide Reaction with Alcohols	44
Reactions of Metal Alkoxides with <i>n</i> -Diketones	44
Reactions of Metal Alkoxides with Alkanolamines	45
Role of Acid and Base Catalysts	46

Orientation	47
Aging	48
Drying	51
Constant rate stage	51
The first falling stage	54
The second falling stage	55
Dehydration	56
Thermal Dehydration	56
Chemical Dehydration	57
Swelling	59
Volume swelling of amorphous materials	61
Swelling of crystalline materials	61
Response of amorphous materials	62
Solid-state mechanism	62
4 COMPOSITE MATERIALS	79
Definitions and Characteristics	79
Unidirectional Fiber Composites	79
Mechanics of Fiber Composites	79
Mechanics of Unidirectional Continuous-Fiber Composites	80
Mechanics of Continuous-Fiber	80
Fiber Composites	80
Failure of Unidirectional Composites Under Longitudinal Tensile Load	81
Failure Processes	81
5 EXPERIMENTAL PROCEDURE	97
Molten- <i>Sci</i> Preparation	97
Filter Spinning and Aging	97
Testing and Characterization	98
6 RESULTS AND DISCUSSION	109
Chapter Outline	109
Chemical Processing of Molten- <i>Sci</i> and Rheology Study	109
Effect of Shear Stress and Crosshead	110
Spinning Condition	110
Change of Rheological Conditions with Time	111
Shear Stress Effect on Molten- <i>Sci</i> Rheology	112
The Role of <i>B</i> Value	112

Thermal Analysis Study	108
Aging Study	127
Densification Study	144
Crosslink Point Determination	149
Glass Transition Temperature	150
Gross Growth Study	167
Tensile Strength Measurements	171
Compression Study	173
I. SUMMARY, CONCLUSIONS AND FUTURE WORK	179
Conclusion	179
Future Work	179
REFERENCES	179
BIOGRAPHICAL SKETCH	184

*Abstract of Dissertation Presented to the Graduate School
of the University of Florida in Partial Fulfillment of the
Requirements for the Degree of Doctor of Philosophy*

3D-CELL PRODUCTION OF CONTINUOUS MULLITE FIBERS

By

SALWAN AL-ASSAFI

December, 1994

Chairperson: Dr. Joseph H. Sauer
Major Department: Materials Science and Engineering

There is an increasing demand for materials that can withstand high temperatures without a deterioration in mechanical properties. Incorporation of fibers in metal or ceramic matrices can provide components that can tolerate their integrity at high operating temperatures. Mullite fibers are a good candidate for such applications. Continuous fibers are a better choice for heat treating applications, as they provide higher strength than short fibers. Achieving continuous spinability and producing glass free mullite fibers presented a challenge to researchers in the past.

The goal of this study was to determine the parameters necessary to produce a glass-free fibers with the ability to achieve continuous spinability. To accomplish the goal, several experiments were conducted. The rheological conditions for continuous spinability and the different factors that control the rheological behavior of the sol were determined. The optimum value for diluting agent/ultramarine

product under nine was determined. The effect of chelating agent on audite crystallization was investigated. Also, the role of aging and aging temperature in the presence of audite fibers was determined. The effect of the chelating agent on the dissolution behavior and the porosity of the final product was determined. The grain growth of audite fibers was also studied.

It was shown that fiber aging was crucial in achieving good-quality fibers. It was also shown that audite crystallization was enhanced with increasing aging time, and it was shown that fiber grain size decreases with the increase of aging temperature. Also, shorter aging times were required at higher temperatures. Crystallized phase determination showed audite was the only phase present. It was shown that no detectable amounts of intergrowths glass phase were observed in the fibers prepared in this study. In contrast, commercial fibers showed the presence of large intergranular glass phase. It was shown that the activation energy for grain growth was high. Glass growth was not significant for temperatures up to 1200°C for long annealing times (22 hours) or up to 1400°C for short annealing times (1 hour).

CHAPTER 1 INTRODUCTION

The demand for materials that sustain high temperatures (in excess of 1200°C) is increasing progressively. Many high-tech industries, particularly the aerospace industry, have numerous applications for such materials. Ceramic fiber composites have a major role in the manufacturing of composites for high-strength, high-temperature applications. A candidate material for ceramic fibers is mullite. Mullite ($3\text{Al}_2\text{O}_3\text{Si}_2\text{O}_5$) is a crystalline ceramic that has an orthorhombic structure and with an aluminum/silicon molar ratio of 3/2. Mullite has good first-group resistance and strength retention at high temperatures [Akash]. In addition, mullite has good thermal shock resistance and chemical stability.

Sol-gel processing has been used in the production of mullite fibers due to the unique properties made available by using this technique. The sol-gel method permits precise control of properties and microstructure before and after heat treatment. By using this technique, fiber spinning can be accomplished at room temperature. Also, sol-gel processing provides better purity and control over homogeneity when compared to more conventional techniques.

The emphasis of this study was the production of continuous fibers. Continuous fibers are of special interest in heat-treating structural composites.

Continuous fiber composites are generally stronger than short fiber composites when a load is applied in the direction parallel to fiber orientation.

The two primary challenges facing researchers in this area were achieving continuous spinnability and producing fibers without a glass phase. Researchers have been able to produce fully crystalline multi fibers but were unable to achieve continuous spinnability (Yanik²). Commercially available multi fibers are currently prepared with holes (Sewill³). This results in the presence of a glass phase. A glass phase can cause a dramatic deterioration in the mechanical properties of the fiber at high temperatures.

In this study, several experiments were conducted to determine the factors that have an effect on aligned processing of multi fibers. The rate of precipitating hydroxyl on the periphery of fibers in the green state was studied. In addition, the effect of pre-spinning hydroxyl on the final microstructure of fibers was investigated. The modulus for continuous spinnability for multi sol was also investigated. The various factors that contribute to achieving continuous spinnability and the factors that determine the rheological behavior of the multi sol were determined. The effect of clarifying agents on viscosity reduced, multi transformation, and fiber microstructure was studied. The effect of varying the clarifying agent/clarifier precursor molar ratio on the sol rheology, sol viscosity, and fiber microstructure was also investigated.

Ageing of multi green fiber in based on in different temperatures was studied. The effect of aging on the properties and the microstructure of fibers was

determined. The role of aging on cellulose formation was also investigated. In addition, the role of aging temperature on fiber microstructure and properties, and the advantages of high temperature aging were determined. Also, the densification behavior of aged fibers was determined.

The process of an intergranular glass phase was investigated. A comparison between the conventional fibers and the fibers produced in this study was carried out to ascertain if there were differences in the intergranular glass phase content. The final study was on graft growth of cellulose fibers. Graft growth as a function of time and temperature was determined.

Statement of Problem

To investigate the critical factors and their underlying mechanisms in the fabrication of single phase cellulose fibers by a method of continuous spinning

Objectives

The objectives of this study were as follows:

- 1- Determine the conditions for continuous spinning by cellulose and study the different factors that affect the rheology of the sol.
- 2- Determine the effect of precipitating hydrolysis on fiber properties and microstructure.
- 3- Study the effect of chain-carrying agent on organic solvent, cellulose formation, and fiber microstructure.

- 4- Determine the optimum chlorine monofluoride precursor molar ratio.
- 5- Determine the effect of aging on mullite transformation. In addition, study the effect of aging on fiber microstructure and properties.
- 6- Investigate the effect of aging temperature on the properties and microstructure of fibers.
- 7- Determine the densification behavior of fibers.
- 8- Determine the factors critical to mullite phase formation and reaction after aging.
- 9- Determine if the fibers produced contain an intergranular glass phase and compare the results to those for commercial fibers.
- 10- Study grain growth as a function of time and temperature.

CHAPTER 2: LITERATURE SURVEY

Mullite Formation Via Sol-Gel

This study addresses the formation of mullite fibers using a sol-gel-based approach. Sol-gel processing was selected because of its unique characteristics which include uniform homogeneity, high purity, and low preparation temperatures [Mao02]. Large crystalline, residual carbon (from sol components), and impure fiber materials are the main disadvantages. Mullite can be prepared using sol-gel from either single phase or biphasic gels.

Biphasic Gels

Gels that contain two different phases are often called biphasic gels. Mullite formation in biphasic gels utilizes a diffusion-controlled growth mechanism by which the diffusion of the Al_2O_3 and SiO_2 components across the reaction layer controls the reaction rate [Li98a]. Aluminous species near the alumina particle surface diffuse along the mullite/alu-mullite interface and react with the excess available silicon species [Hu2004]. Silicon species may diffuse in the opposite direction toward alumina species. Mullite crystals form on the interface and grow toward the biphasic region. The growth rate of the mullite is limited by a slow-step transportation rate and the amount of the reaction. The mullite formation

temperature for this type of gel is high, about 125°C, compared to other approaches.

Diphobia gels were prepared by Prochazka and Klap [Prog3]. The aluminum precursor was aluminum isopropoxide, and the silicon precursor was ethylphenylsilanol. Both precursors were dissolved separately in cyclohexane. Appropriate volumes of the solution corresponding to the desired aluminum:silicon composition were measured and mixed in a blender. Fifty-five grams of water per mole of each alkoxide was mixed with twice its volume of isopropylalcohol and added to the cyclohexane solution. The resulting sol was agitated then aged for 24 hr. The solvent was evaporated at room temperature, and the mixture was dried at 125°C. The resulting powder was reduced at 750°C.

The amount of residual carbon was observed to decrease with increasing heating rate. The diphobia gels prepared by this method were amorphous up to 950°C where the formation of a crystalline phase was observed. The crystalline phase was determined to be either γ -alumina or an α -Al₂O₃ spinel. Melting temperature was denoted at 1300°C.

Fink, Tolksa and co-workers used metal alkoxide to make diphobia gels [Prog4]. The aluminum sol was made by hydrolysis and polycondensation of $Al(OCH_3)_3$ (aluminum-tert-butoxide) followed by a peptization step. The resulting sol was a clear aqueous sol which contained $Al(OCH_3)_3$ colloidal particles. These particles were treated with $Si(OCH_3)_4$ (tetraethyl orthosilicate) in water-ethanol medium forming a closely-linked silica layer around and in between the

particles. Cracking occurred after a short period of time yielding irregular granules about 1 mm in size upon drying at 500°C for 30 min.

Differential thermal analysis (DTA) results showed a shallow endothermic peak between 400°C - 1000°C which was caused by the gradual loss of hydroxyl groups. Broad diffraction peaks for quartz were observed using x-ray diffraction analysis (XRD) in a sample heated to 1000°C. A mullite formation endothermic differential thermal analysis (DTA) peak was observed at 1287°C. Upon heating to 1287°C, the grains had a prismatic shape and a glass phase was present, predominantly at the triple points.

Mullite was also prepared from a diaphase gel by Basal et al. [1997]. A boehmite gel was prepared using γ -Al₂O₃, while the alumina gel was prepared using anatase SiO_2 . The mixture of the two gels was gelled at a pH of 9. The gelation rate was controlled by the addition of hydrochloric acid (HCl). Larger addition of HCl resulted in larger gelation [1997]. The dried gel was ground in an alumina-lined ball mill and calcined at 1400°C. The mullite formed was surface milled using diamond tools. The DTA showed the crystallization of mullite at temperatures above 1200°C. The green compact of mullite powder were isostatically pressed in a pressure of 200 MPa and sintered at a temperature of 1300°C. Transmission electron microscopy (TEM) micrographs for sintered ball-milled mullite showed traces of a glass phase but no glassy points at triple points.

Aluminosilicate gel with $\text{Al}_2\text{O}_3/\text{SiO}_2$ composition ratio = 1, 1.5, and 2 were prepared by Wu and Hollins [2002]. The powders used were collected

potassium-benzoate (KOBH) and terephyl-oxalocetate (TBKO). The TBKO, ethanol, and water with KOBH (10C) were mixed together in a ratio of 50 wt% : 30 wt% : 20 wt%. After the mixture was aged in a 50°C bath for 2 h, the colloidal potassium-benzoate sol was centrifuged, and mixed for 30 min. The mixture was then aged in a 50°C water bath. After 24 h, the mixture formed a translucent white gel.

It was observed that the two distinct phases, potassium-benzoate, and amorphous silica, transformed independently up to 1200°C, then reacted to form silica directly without the formation of a precursor (mesophase or liquid phase). Meltex was formed via nucleation and growth of single crystal grains by a process that was either reaction or short range diffusion controlled (Wen 1996). It was found that the growth rate was time-dependent. The origin of the time-dependent character of the growth rate was not explained. It was also shown that Al_2O_3 particles that were larger than 20 nm did not react completely with SiO_2 , particularly at low temperatures. These alumina particles appeared to be entrapped in the meltex phase. Although the overall composition was stoichiometric, the transformation product was a silica + meltex mixture with entrained alumina particles.

Bundschuh and Alsay attempted to explain the time dependence of the growth rate found in the 'Aix and Hultzen' reaction (1995). They argued that the growth rate of the meltex grains was controlled by the dissolution of alumina particles into the mesophase phase. When considering entrainment of alumina particles by the growing meltex grains, the number of transitional alumina grains

restating as the diffraction pattern decreases slowly with time. Consequently, the initial rate of alumina dissolution into the amorphous phase was not constant, but decreased slowly with time. The resulting isothermal dissolution rate for mullite glass.

Mullite glass gels were also prepared by Beopoulos (1968). Two processing methods were investigated. In both methods, the mullite gel was prepared by dispersing colloids of TiO_2 and an aluminum monohydrosilicate ($\text{AlO}_2\text{Si}(\text{OH})_4$) sol. The aluminum monohydrosilicate sol was prepared by dispersing boehmite powder in an aqueous solution using 10% and 15% per mol of aluminum monohydrosilicate. In the first method, the sol mixture was stirred in the acidic condition and gelation was completed. In the second method, gelation was performed by the addition of a few drops of 0.1 M NH_4OH into the acidic aluminum monohydrosilicate + TiO_2 sol. Both approaches to large or 25 to 30 μm were formed spontaneously.

Differential thermal analysis x-ray diffraction results showed that mullite formation occurs at a relatively high temperature (1200°C). The XRD analysis showed the presence of an amorphous phase and spodumene phase below the 1200°C isothermal. The high mullite formation temperature enabled recrystallization to occur at temperatures as high as 1200°C. As a result, high densities may be achieved. Upon heating at 1200°C, 99% of theoretical density was achieved in the first method, while a reduced pressure of 44.1 MPa was needed to achieve the same density in the second method. The XRD patterns for samples from the first method showed the presence of a glass phase and a spodumene together with mullite after

heating at 1200°C. No glass phase was detected in samples treated similarly from the second method.

A technique similar to the one developed by Romprik was used by Li and Thompson (1990a). The diaphane gel was prepared by dispersing boehmite powder in a dilute HNO_3 solution. A suitable amount of TiO_2 together with an equal volume of ethanol were mixed with the boehmite dispersion to give the stoichiometric ratio of alumina/titania molar. Gelation was accomplished in 22 hr heating at 100°C oven. Diffractometry (DIA3000) results showed that the silica phase in the diaphane gel remained amorphous throughout the heating process and reacted with alumina to form mullite at 1200°C. The boehmite gel experienced the following transformation:



Li and Thompson showed that mullite formation followed an Avrami-type, diffusion-controlled growth mechanism with the nucleation process was amorphous alumina grain boundary melt phase. Samples fired at 1200°C showed rod-like mullite.

Second diaphane mullite gels were studied by Kline and Langford (1990b). The mullite mulls were prepared by calcining mullite gel at 1400°C for 2 hr. The mullite gel was prepared by precipitating granular boehmite and colloidal silica and gelating the sol using acetic acid. A 50-molar-mole dispersion of calcined mullite powder was ball-milled and sonicated to yield an agglomerate-free suspension of fine sand particles.

Swelled gels were produced by associating different amounts of the melt composition to the resulting sol (either polymerase was cured out). The sol was then gelled and dried at 160°C. The microstructure of the associated gel was compared to the microstructure of the uncured gel after being at 1200°C. More pores were observed in the case of uncured gel, while gels treated with 4 wt% malite had showed expanded grains. No evidence of interpenetrating phase phase was found in the case of treated gels.

A malite seed quantity of 8.125 wt% gave different results. Small grain and smaller grains having aspect ratios as high as 12.1. The rest of the sample was a mass of fine, nearly equiaxed grains with some intergranular porosity. The large grains resembled whiskers in a fiber-grained mass. It was not confirmed if the presence of the elongated fibers reinforced the material.

The effect of precursor composition on molite formation and the resulting structure was investigated by Li and Thomson [Li97]. Diphasic gels with Al/In atomic ratios of 4/1, 3.1/1, 2/1, 1/1, and 1/2/1 were used. Molite formation was measured at about 1200°C for all samples with only slight differences in temperature. The molite formation temperature was a minimum for an Al/In ratio of 3.1/1 and increased as the Al/In ratio of the gel increased or decreased. In the case of 4/1 gel, dissolution of alumina was the molite solid solution was observed after the initial molite formation. The dissolution was reversed above 1150°C with the formation of $\beta\text{-Al}_2\text{O}_5$ and then $\alpha\text{-Al}_2\text{O}_5$. A change of microstructure from equiaxed

No elongated malleus glass structure was observed within a narrow range of temperatures near the 40% melt of 5%.

Li and Thomas developed another process to produce diaphane gels. The silica sol was prepared by hydrolyzing TEOS in water and a silicic acid solution with a pH of 1 (Li²Mo₃). After hydrolysis was completed, aluminum nitrate was introduced. The solution was gelled in a sealed container at 100°C for 1 day. Malleus formation of the gel was detected above 1200°C. A 100°C peak observed in the DTA curve was attributed to the formation of Al₂Si spinel anorthite malleus.

Single-Phase Gels

Gels that have molecular scale mixing of the components are referred to as single-phase gels. For malleus, single-phase gels have molecular-scale mixing of alumina and silica through either coprecipitation of alumina and silica salts or hydrolysis of metal alkoxides [Li²Mo₃]. Malleus formation exhibits a nucleation-controlled mechanism. The malleus transformation temperature for single-phase gels is below 1000°C.

One of the major obstacles to making homogeneous single-phase (polymeric) malleus gel is the equilibrium difference in the hydrolysis and self-condensation rates of alumina and silica alkoxides. Silica alkoxide hydrolyzes at a much slower rate than alumina alkoxide [Takagi]. Inhomogeneity arises from the formation of heteropolymer that do not have malleus malleusinity.

A process was developed by Yodkin and Parker to circumvent the hydrolysis rate difference problem [Yod84]. The silicon alkoxide was partially hydrolyzed while the aluminum alkoxide was not hydrolyzed. Upon the addition of the aluminum alkoxide to the silicon sol, a white precipitate formed, but this coagulates dissolved forming a clear solution within hours at 60°C. The final hydrolysis was carried out either in the liquid state by mixing water, which resulted in the formation of a gel or fine powder, or in the solid state after the sol was dried by evaporation or the deposition of thin films.

Mullite formation was observed to occur at 980°C in EDX measurements. Also, a large spontaneous densification occurred at 940°C. The low mullite formation temperature was attributed to the intimacy and homogeneity of aluminum bonding. The microstructure consisted of equigranular mullite grains about 14 microns in size, with no evidence of a secondary amorphous phase [Yod87].

Sparks and Tacke developed a process to produce sprayable aluminum silicate [Spa82]. The process consisted of two hydrolysis steps. In the first hydrolysis step, aluminum propionate monomer acid silanol was mixed with isopropyl alcohol, water and hydrochloric acid in a ratio of 1.0:1.0:1.0. To prevent the formation of precipitates, half of the alcohol was used to dilute the metal alkoxide, while the other half was mixed with the water and acid which was then slowly added to the alkoxide mixture. Thiamalate, isopropyl alcohol, water, and hydrochloric acid in the molar ratio of 1.0:1.0:0.1 were added dropwise to the aluminum sol in the second hydrolysis step.

After allowing the sol to gel in air, crystallinity was observed. The gel was dried at 100°C after being dried at 100°C. Analysis via XRD showed that mullite was the only phase found. The microstructure of the dried material and the presence of glass phase were not discussed in this study.

Li and Thomson also developed a process to produce single-phase mullite gel [Li90a]. The aluminum precursor, $\text{Al}(\text{OH}_2)_3\text{H}_2\text{O}$, was dissolved in absolute ethanol. The solution was mixed with tetraethyl orthosilicate. The mixture was then gelled at 40°C over a period of two weeks.

Dynamical x-ray diffraction (DAXRD) results showed that the gel was completely amorphous up to approximately 1000°C, where mullite began to form. Mullite was the only crystalline phase detected, and the formation of a mullite glass phase was not observed. Fourier transform IR and FT-IR analysis showed that at 100°C the gel has a mixture of amorphous silica and alumina, and at 1000°C Al-O-Si bond formation was observed. Transmission electron microscopy (TEM) and BET results for powder heated at 900°C showed an average particle size of about 33 nm [Li90a].

Wolny and Strunz did a study on single-phase gels derived from an aluminum borate hydrolyzed in THF molecular sol [Wolny and Strunz]. Two types of gel were prepared: fresh gel and aged gel. The fresh gel was prepared by rapid droplet drying of the molecular sol at a heating treatment to 100°C. The aged gel was prepared from the fresh gel by exposing it to a heating treatment at 100°C.

Differential thermal analysis of the fresh gel showed an exothermic peak at 1000°C [Wolny and Strunz]. X-ray diffraction analysis for samples heated just above 1000°C

showed nearly complete crystallization to the alumina with tetragonal mullite ($\text{3Al}_2\text{O}_5\text{SiO}_4$). Analysis using EDX showed the presence of a minor amorphous phase enveloped by tetragonal mullite.

Differential thermal analysis of the aged gel showed a prominent exothermic peak at 980°C . In addition, a broad peak was observed at 147°C . X-ray diffraction analysis of samples heated just below and just above 147°C showed that the EDX peak at the temperature corresponded to crystallization of 10 wt\% aluminothermum mullite ($\text{3Al}_2\text{O}_5\text{SiO}_4\text{.}2\text{Al}_2\text{O}_3$). It was observed that by decreasing the heating rate at which the DTA was performed, the 147°C peak shifted to lower temperatures. Further, while the intensity of the 147°C peak increased with higher heating rates, the intensity of the 980°C peak decreased.

Single phase gels were also prepared by Schaefer and co-workers [16,17]. Aluminotherm mullite (10 wt%) was mixed with T80% (20 wt%) in the presence of tetragonal mullite. Water was added dropwise to the mixture, and a white gel was produced. Differential thermal analysis showed a sharp exotherm of high intensity at 980°C , in addition to a weak exotherm at 147°C . X-ray diffraction analysis for samples heated at 1400°C showed the presence of γ - Al_2O_3 mullite, and small amounts of anatase. Mullite was the only phase observed for samples subsequently heated to 1400°C and 1600°C .

The use of devolatilizing agents in the processing of single phase mullite gels was studied by Hennach and co-workers [18,19]. Their system consisted of aluminumoether, β -diketonate, trisilylorthosilicate, tetrapropyl and hydroxylamine and,

Acrylonitrile(Acry), methylacrylate(MA), and methylmethacrylate(MMA) were used as the α -dienes. The molar ratio, R , of β -diketone to aluminum-oleylates was varied from 0.5 to 2.0. A solution of β -diketone and bispropylene was added dropwise to the aluminum-oleylates solution. A solution of TGAII and bispropylene was added thereto. Bisphenol was purified by adding an aqueous NaOH solution.

It was shown that particle size was a function of the amount of β -diketone used. The particle radius measured was a function of the number of condensation sites per aluminum atom which were blocked by β -diketone after hydrolysis. The more condensation sites blocked the smaller the particles.

The gelation time was found to be dependent on the amount and type of capping agent. The gelation time increased as the amount of β -diketone increased and the larger the molecular size of the capping agent. Nuclear magnetic resonance (NMR) results showed the presence of Al-O-C₂H₅ bonds during all stages of gelation. The ¹³C-NMR spectra showed that it was possible to obtain homogeneous gels on a molecular scale using cationized aluminum clusters.

Continuous Melted Fibers Using Sol-Gel Processing

The main problem associated with sol-gel processing is the difficulty in producing large shapes because of the cracking experienced by drying structures associated with capillary forces, and shrinkage stresses during drying [Lu(1991)]. These effects are minimized with fibers because the diffusion distance is small and

stress can be relieved by heat treating of the fiber. These factors are effective after forming the fibers from the sol, however, formation of fibers from the gel is a difficult task. Production of good quality continuous carbon fiber requires achieving certain rheological conditions that are essential for continuous spinning.

Prior to the use of sol-gel processing, carbon fibers were produced from carbon fibers [Seki et al]. The liquid phase required spinnability properties in entangle spinning of fibers. As a result, composition was limited to certain amounts in mixture of carbon. Consequently, high percentages of SiC were often needed in the fibers, and this limited their use at high temperatures.

Sol-gel processes can be used to produce fibers in the sol stage. This extends the range of compositions of carbon fibers to include a variety of compositions that were not possible using the melt method. As a result, fibers that possess good environmental, chemical, durability, and high tensile strength can be produced. Another advantage of sol-gel processing of fibers over spinning of carbon nanotubes is the lower processing temperature. Fiber spinning using the sol-gel method is usually carried out at room temperature which is more economical and technically more controllable than high temperature spinning.

Hochst and co-workers investigated the processing of continuous carbon fiber from polymeric sols [Hoch et al]. The first step in the process was the production of polydiaminotetraamine. The polydiaminotetraamine was prepared by partially hydrolyzing and polymerizing an aliphatic diamine: Tetrahydrohexaazocine was polymerized in ether with an aqueous excess of water which was added dropwise at 20-40°C. The

polymerization process, was measured by monitoring the amount of C_2H_6 produced. The degree of polymerization was controlled by changing the amount of water added. A polymerization sol was then mixed with the polydimethylsiloxane to form a silica sol.

The amount of silica-containing compound to be mixed with the solution of the polydimethylsiloxane was found to affect the spinning of the sol. When a silanol containing compound with no spinnability was added in large amounts to the polydimethylsiloxane, the spinnability of the resulting solution was poor.

The resulting sol was spun through 70-100 micron holes. The atmosphere in which the spinning was carried out was sterilized. Solvents contained in the fiber were removed during or after the spinning step. The spun fibers were hydrolyzed by heating dissolved in the sol, and then were dried for the purpose of stabilization and curing. Fibers prepared at temperatures below 1250°C had good strength. On the other hand, fibers dried at the 1250°C-1350°C range were brittle and had low strength due to an exaggerated growth of needle grains. As a result, the use of these fibers at high temperatures was limited.

Kurn and Sorenson investigated the processing of continuous melton fibers from aqueous gels [Ku77]. The melton sol was prepared by adding aluminum isopropylate to a mixture of formic acid and distilled water. Aluminum hydroxide was added to the mixture with subsequent heating to 80°C until the solution was clear. Following this, aqueous colloidal titanium, aqueous colloidal silica, and latex and were added to the mixture. The resulting sol was then concentrated under a blanket. The sol was filtered through a spinneret after the

spinning viscosity was observed. The extruded fibers were drawn vertically downward through the center of a dry bath in a countercurrent stream of dry air introduced near the bottom end of the track. The fibers were then fixed at 200°C to remove physical water and other volatiles. Following initial drying, the fibers were heated to 350°C to remove residual volatiles and reduce crystallization. After heating to 350°C, a toluene solution of 0.5 wt% tetraethoxysilane (Meldrum polymer rubber) and 2.0 wt% mineral oil was applied to the fibers before winding them on a drum.

Samples fixed at 1500°C had a tensile strength of about 2.0 GPa. X-ray diffraction analysis showed that fibers fixed at 1500°C for less than 10 sec, showed a molten phase with traces of silicon. After periods of time longer than 15 sec at 1500°C, silicon was the only phase detected.

Processing of continuous molten fibers was also investigated by Becker and co-workers [Tachik]. The silica sol was prepared by hydrolyzing TEOS. The hydrolysis step was carried out in the presence of distilled water, hydrochloric acid, and tetrapropyl silanol. The mixture was allowed to react at 40°C for 30 min. Hydrolysis of the silicic acid was followed. The silicic acid precursor was then an oligopeptidyl siloxane over silica (ADS). The silica provides a greater possibility for the formation of the linear polymer necessary for production of a spinable fiber, as it allows low reaction rates for the ADS. The silicic acid components, ADS, hydrochloric acid, water, and tetrapropyl silanol, were mixed slowly to form a homogeneous mixture. The mixture and silica sol were then mixed at

40°C in a nitrogen atmosphere. Specimens were retained from the test at time periods ranging from 8 hours to 3 days.

In the spinning process, the fibers, after being extruded, were passed through an air gap in a bath containing deionized water and polyethylene oxide. The pH of the bath was adjusted by adding sodium hydroxide. The bath was used to regulate the fibers and to improve the structural integrity. Fibers with a large diameter, 110 microns, were spun. After being at 1000°C pure carbon fibers were obtained. However, the fibers exhibited porosity and microvoids, and were very brittle, as a result.

The use of diphenol gel to produce carbon fibers was studied using two methods by Venkatesan et al. (1986). The two methods differed in the choice of precursor materials used as the source of carbon and silica. Aluminum hydroxylsilicate hydride and LiUDOPS-AB colloidal silica were the starting materials for method I. Aluminum formate and LiUDOPS-CTI colloidal silica were the starting materials for method II. Another pertaining difference was that in method I fibers were drawn by hand, while in method II, fibers were prepared by controlled spinning.

Gas adsorption measurement indicated that the average pore size for method I fibers heat at 1000°C was about 4 nm. An average pore size of 2.3 nm was observed for method II fibers heat at 800°C. The fiber pore structure of method II resulted in a more rapid densification. It was believed that densification of fibers occurred by a direct fiber mechanism in both methods.

X-ray diffraction analysis showed that mullite transformation occurred above 1200°C for both methods. Fibers from both methods fired at 1200°C showed grain size below 1 μm . Examination of grain boundaries of method 1 fibers via TEM did not show the presence of a glassy phase, so similar analysis was done on method 2 fibers. However, neither method could be used to produce solutions with the necessary properties for continuous fiber spinning.

Barbier and co-workers investigated the effect of additives on microstructure and crystallization of mullite [Ref.11]. The alumina sol was made by dissolving alumina powder in a mixture of methylene sulfide. A commercial silane sol, MALEO HDMA, was added to the alumina sol. The additives investigated were Ba_2O_3 , P_2O_5 , and Ca_2O_3 . They were added as basic salt, phosphorus acid, and aluminum acetate, respectively. Lanthan sol was added to either gelatin.

The sol was concentrated to a viscosity of 100 to 150 $\text{mPa}\cdot\text{s}^{-1}$, and then pressure extruded through a spinneret. The fibers were dried after extrusion through a drying chamber to form continuous filaments. Differential thermal analysis was used to determine transformation temperature. For the unmodified mullite fibers, an exothermic reaction with a peak at 1000°C was confirmed by XRD to correspond to the formation of a spinel phase. A second exotherm observed at 1200°C was confirmed to correspond to mullite formation.

Addition of low temperature glass formers such as Ba_2O_3 and P_2O_5 produced sharper exotherms and raised the spinel formation temperature to 1011°C and 1014°C, respectively. On the other hand, the addition of Ba_2O_3 and P_2O_5 lowered the mullite

formation temperatures are 1222 °C and 1232 °C, respectively. Addition of Cr_2O_3 did not appear to have an effect on spall and molten formation temperatures.

Transmission electron microscopy micrographs of the uncoated molten fibers heated to 1230 °C and held for 1 hr showed grain size of 4000 Å, intergranular pore size of 250 Å, and average intergranular pore size of 300 Å. Fibers that contained Fe_2O_3 had the smallest grains and the most uniform granular distribution. Grain sizes of 800-1000 Å, and pore size of 300 Å were observed for fibers containing Fe_2O_3 . In addition, Fe_2O_3 fibers were denser than those of any other composition studied. On the other hand, addition of Cr_2O_3 or ($\text{Fe}_2\text{O}_3 + \text{Cr}_2\text{O}_3$) resulted in grain size larger than that of the uncoated molten fibers.

Kim and co-workers studied formation of molten fibers from polymeric salts [Kim02]. The starting salt was prepared by mixing chloroform terephthalate with isopropanol, and tetrahydrofuran. The mixture was then hydrolyzed and polymerized by adding water and hydrochloric acid. The salt was prepared by mixing TMCDA, isopropanol, water, and hydrochloric acid. After mixing the two salts, a cocondensation step was carried out inside an 80°C oven for 50 hr. The cocondensation time was reduced to 24 hr by using a rotary vacuum evaporator and a vacuum drying oven. Extrusion of fibers was accomplished by drawing fibers through a 200-400 μm hole spacers.

Viscosity measurements of the molten salt revealed that by the incorporation to chloroform-terephthalate molar ratio (R) of 1.5, the viscosity increased dramatically after 50 hr. General increase in the viscosity was observed for R values of 1.5 and

6.1. The rheological behavior of the soil as a function of time was determined. Shear thickening behavior was observed after 40 hr, rheotropus behavior after 50 hr, and a pseudoplastic or shear thinning flow behavior after 160 hr.

Differential thermal analysis results indicated that mullite formed in-situ at 1300°C. X-ray diffraction analysis for samples heated to 1300°C showed the presence of a mullite phase. Micrographs taken by SPM showed that the fibers had a needle like microstructure.

Commercially Available Mullite Fibers

Mullit 400 and 440 are among the commercially available mullite fibers. Mullit 440 fibers consist 70% Al_2O_3 + 20% SiO_2 + 10% MgO [Jewell]. They have a tensile strength of 1.72 GPa and modulus of elasticity of 107.241 GPa. Fibers heat treated to temperatures up to 1600°C retained their strength. Fibers heat treated beyond 1400°C showed a significant degradation of properties. Mullit 400 fibers contain very small crystallites in the range of 20 to 60 nm in size.

Mullit 400 fibers have a 3 to 2 molar ratio of aluminum to silica [Jewell]. The average grain size was shown to be 150 nm. The fibers retained about 55% of their strength through a heat treatment temperature of 1600°C, and 60% strength retention after 1400°C (these fibers were tested at room temperature). High temperature strength measurements showed that the strength remained almost constant up to about 1600°C then fell to about 50% of its initial level at 1700°C. The fiber strength at 1250°C was about 6.3 GPa. The measurement of the elastic

modulus at high temperatures showed a significant drop above 800°C. At 1000°C, the modulus was approximately 10% of its initial value. Thus fibers show a distinct amorphous glass phase.

Two alumina-alum fibers were developed by Bauschert chemicals. The composition of the fibers is 85 with alumina and 15 with silica [Lew98]. The microstructure consists of very small $\gamma\text{-Al}_2\text{O}_5$ crystallites homogeneously mixed with an amorphous silica phase. The fibers were processed by polymerization of metal alkoxides. The fibers were heated to 700°C to remove organic. The final step was heating the fibers to 900°C to complete the formation of $\gamma\text{-Al}_2\text{O}_5$.

High temperature strength and elastic modulus measurements showed a drop in the strength and the modulus above 800°C. The elastic modulus at 1000°C was about 40% of its original value. Measurements of the creep rate indicated that the fiber crept at temperatures above 800°C, and that the creep rate increased rapidly with temperature. The degradation in the mechanical properties was attributed to the softening of the amorphous silica matrix in which the alumina crystallites were embedded. Transformation to molten was noted for fibers heated above 1120°C.

CHAPTER 3 SOL-GEL PROCESSING

Introduction

The term sol-gel is used to describe a variety of chemical synthesis of inorganic materials. The process owes its name to the liquid-crystalline structure that occurs after sol formation or during aging [Bard]. The sol is a system in which separate dispersed species (solutes and solvent) are extensile. If the solvent- or suspension conditions are changed slightly, destabilization can occur [Bard]. The destabilization of the sol can result in precipitation of the sol species or aggregated or aggregated particles in the formation of a homogeneous gel.

The gel consists of a continuous solid network enclosing a continuous liquid phase [Bard]. The gel has an elastic character which is introduced by the continuous solid network. The sol-gel technique involves physical and chemical processes associated with hydrolysis, polycondensation, drying, dehydroxylation, and crystallization. The advantages associated with sol-gel processing are [Bard]:

- very high purity,
- better homogeneity compared to powder mixing technology,
- low processing temperature compared to traditional ceramic processing techniques,
- uniform phase distribution in multicomponent systems,
- easy preparation of coatings and thin films,

- better size control in powder synthesis, and
- the ability to produce fine crystalline and nanocrystalline solids.

Although sol-gel processing has many advantages, it also has some disadvantages, such as [Mark2]

- the high cost of the materials,
- large sludge during processing,
- limited porosity,
- isolated hydroxyl groups and carbon,
- health hazards associated with the organic components, and
- long processing times.

Sol can be divided into two major categories, colloidal (particulate) sols and macromolecular (polymeric) sols. A colloidal sol is a solution that contains discrete particles [Bard2 and Bard3]. A macromolecular sol is a mixture of macromolecules that are obtained by the hydrolysis and polymerization of metal alkoxides.

Colloids are solid particles with diameter of 1 nm to 100 nm [Wu08]. A colloidal system is a dispersed or heterogeneous system consisting of at least two phases, one of which is a dispersed phase and is uniformly distributed within a continuous phase (the dispersion medium) [Wu08].

A polymer, or a macromolecule, is a large molecule formed from monomers that are capable of forming at least two bonds [Mark2]. Metal alkoxides ($M(OEt)_3$) are derivatives of alkoxide [K038] in which the hydrogen of the hydroxyl group has been

replaced by a metal (M). Metal oxides can also be considered as derivatives of metal hydroxides, $M(OH)_x$ [26,27]. Colloid stability is an important issue in the processing of colloidal soils. An understanding of the different forces acting on the colloids is essential when studying the stability of colloidal soils.

Stability of Colloidal Soils

The stability of colloidal soils is a function of a number of factors. These factors are presented in the following sections.

Surface Energy

From the first and the second law of thermodynamics, for systems with a phase interface separating the bulk phases [28,29]:

$$\delta U = T \delta S - P \delta V + \gamma \delta A + \sum \mu_i \delta n_i \quad (1)$$

where:

U = internal energy,

T = temperature, S = entropy,

P = pressure, V = volume,

γ = surface tension, A = surface area,

μ_i = chemical potential of element i ,

and n_i = number of atoms of element i .

Introducing the Gibbs free energy G , where G is

$$G = H - TS$$

1.2

The derivative of the Gibbs free energy, dG , can be calculated as

$$dG = -SdT + \mu dP + \nu_1 dN_1 + \nu_2 dN_2 \quad 1.3$$

The surface tension of a solid can be defined by the reversible work done in creating a new surface or by adding or removing atoms to or from the surface [Kau96]. The surface tension relative to the free energy and the internal energy can be defined as

$$\gamma = \left(\frac{\partial G}{\partial A} \right)_{T, P, \nu_1, \nu_2} = \left(\frac{\partial U}{\partial A} \right)_{T, P, \nu_1, \nu_2} \quad 1.4$$

Where γ represents the partial derivative, and the subscripts refer to the independent variables which have to remain constant during the increase in surface area by a unit amount.

The source of the surface free energy arises from the broken or distorted bonds of surface atoms. These atoms are only partially surrounded by neighbouring val. atoms. These broken or distorted bonds result in an increase in surface energy [Kau96].

From the above discussion it can be seen that the higher the surface area, the higher the energy state of the surface particles. Since systems tend to maintain a low energy state, there is a tendency to Min. the surface area.

As mentioned earlier, colloids are very small solid particles with diameters of $1 - 100$ nm. Assuming that the colloids are spherical, the surface area to mass ratio is

$$\frac{SA}{M} = \frac{4\pi r^2}{\rho V} \quad (3.3)$$

Where SA is the surface area, M is the mass, ρ is the density, and r is the radius. This means that for the same mass, the surface area of two spheres is larger than the surface area of one sphere. Therefore, there is a tendency for the colloid in the solvent to collapse, or to move to one another and coalesce to reduce surface area, and as a result, reduce the surface energy [Jacob].

The process of coalescence is driven by the difference in the solubility between surfaces of different extensions. Particle surfaces have positive rods of curvature, while neck regions (formed during coalescence) have negative rods of curvature. The solubility is related to the radius of curvature by [Drozd]

$$S = S_{\infty} \exp \left(\frac{2\pi\gamma R_{\infty}}{kT} \right) \quad (3.4)$$

where

S_{∞} = solubility of a flat surface of the solid phase

γ_{SL} = solid-liquid interfacial energy

R_{∞} = under radius of the solid

k = gas constant

T = Temperature

r = particle radius

This equation shows that positive radii have high stability while negative radii have low stability. As a result, the enthalpy decreases from the particle surface and precipitates in the neck region. This process is similar to the desorption-condensation process which will be discussed later in this study.

Colloid or suspension exhibit Brownian motion. Brownian motion is stimulated by the constant collision of liquid molecules with colloid [36-38]. The effect of these collisions on the movement of the colloid is inversely proportional to the size of the colloid. These moving colloid collide with each other and they may stick to each other due to the strong Van der Waals attractive forces.

Van der Waals Forces

"Van der Waals forces are short range secondary attraction forces which originate through electron-dipole bonds or on the surface of a material." [39-41]. In an electrical dipole, the centers of negative and positive charges are displaced with respect to each other. The presence of displaced center of charges allow the cohesive forces to become temporary. Electrical dipoles are either inherent or induced. Electrical dipoles are inherent in asymmetric molecules. Dipoles can be induced by an electric field due to either applied externally or applied by a neighboring ion, molecule or atom. The dipoles that have symmetrical structures

develop Van der Waals interactions. Van der Waals interaction forces are relatively weak for induced dipoles. Another type of dipole is the temporary dipole.

The Van der Waals forces result from three types of interactions (Debye and Flory):

- permanent dipole with permanent dipole (Keesom forces),
- permanent dipole with induced dipole (Debye forces), and
- induced dipole with induced dipole (London forces).

The third interaction occurs only when two atoms are in close proximity. The electrons of the two atoms will redistribute relative to maximize the energy of the system, producing two dipoles and resulting in a net attraction force. The total interaction force between molecules is the sum of all three contributions. The potential energy of attraction two spheres, U_{12} , is [Kro88]:

$$U_{12} = \frac{C_6}{r^6} \quad 31$$

where:

- A. = Hamaker constant
- b. = particle diameter
- r. = separation distance

The Van der Waals attraction forces can result in aggregation upon particle contact. Repulsion forces have to be induced to prevent aggregation of colloids.

Electrostatic Repulsion

The method used to prevent or reduce aggregation is the development of electrostatic repulsion. The net force between particles in suspension is assumed to be the sum of the attractive Van der Waals force and the electrostatic repulsion caused by the induced surface charges. The repulsive barrier depends on the type of ions in the electric double layer. The electric double layer is the region adjacent to the surface of the colloid which contains the charge-determining ions (those positioned on the colloid surface) and the counterions (those positioned on the adjacent surface). The counterions act to neutralise the surface charges.

Surface charges can be altered by the following techniques [BachH]

i- Chemical reaction with an aqueous medium: In this process the sign of the surface charge is determined by the pH of the solution [KroKH]. For hydrous metal, the charge-determining ions are H^+ and OH^- . The charge is reversed by protonating or deprotonating the M(OH) (metal hydroxide) bonds on the surface of the particle. The pH at which the particle is neutrally charged is called point of zero charge (POZ). In the case of pH lower than POZ, i.e. acidic condition, the M(OH) group is protonated and a positive charge is acquired [BachH]



When the pH is greater than the POZ (basic condition), the M(OH) group is deprotonated and a negative charge is acquired



The magnitude of the surface potential, ψ_s , depends on the value of pH relative to PZC.

3- Adsorption of specific ions: In this process, the surface develops a charge due to the preferential adsorption of particular ions from the solution [Jac04]. Ions are adsorbed on oppositely charged surfaces [Jac04]. In some cases, complete adsorption of ions can lead to neutralization of the surface charge, as shown in the reaction:



The adsorption of anions may lead to surface charge reversal:



Where $\text{M}^{\text{+}}$ is Cl^- .

3- Desorption and dissociation: This process depends on the difference in the dissociation rate of the different ion in colloid particles [Jac04]. If the colloid is composed of two more species than H^+ it is likely that the anions and cations will dissociate at different rates [Jac04]. The surface will have a high concentration of the ions with the lower dissociation rate, and a low concentration of the ions with the higher dissociation rate. As a result, the charge of the lower dissociation rate ions will dominate the surface charge.

The Structure of The Electro Double Layer

The distribution of ions and polar liquid molecules is influenced by the surface charge of the colloid in solution. Coulomb forces repel like-charged and attract polar liquid molecules and oppositely charged ions into a region near the surface increasing their concentration relative to the average in solution [Kestens]. The potential gradient in the double layer is not sharp, because thermal vibration of molecules in the liquid near the interface of emulsion. The diffusion of counterions due to molecule thermal vibration is more significant at high temperature. The double layer can be divided into two regions, the Stern layer and the Gouy or diffuse double layer [Brett]. The Stern layer is the region adjacent to the charged surface that contains a tightly bound layer of counterions. The diffuse layer is the region beyond the Stern layer in which the counterions and polar liquid molecules diffuse freely. The plane separating the Stern and the Gouy layer is called the Helmholtz plane.

Charged colloids move when an electric field is applied [97-98]. As they move, they carry along the adsorbed layer and part of the counterions cloud. The rest of the counterions (the more distant portion of the double layer) move in the opposite direction. The plane that separates the fluid that moves with the particle from the region that flows freely is called the slip plane or plane of shear. The potential at the shear plane is referred to as the zeta potential. The point at which the pH is equal to zero is referred to as the isoelectric point (IEP) [100].

The potential drops linearly through the Stern layer. A model for the potential gradient in the diffuse double layer was developed by Debye and Hückel (Debye1923). This model is based on a uniformly charged surface, a solvent with uniform dielectric constant, and point charges. Assuming that the distribution of charges in the diffuse layer follows Boltzmann's equation, the concentration of counterions in the diffuse layer, N_0 , relative to the concentration of counterions adsorbed on the surface, N_{ad} , is given by the following ratio:

$$\frac{N_0}{N_{\text{ad}}} = \exp\left(-\frac{U_0}{k_B T}\right) \quad (3.12)$$

where U_0 is the potential energy of the ion, k_B is Boltzmann constant, and T is the temperature.

The potential in the diffuse layer V , where the surface potential $V_0 \leq 100$ mV, can be defined with respect to the surface potential as [Bard1990]

$$V = V_0 \exp\left(-\frac{r}{\lambda^2}\right) \quad (3.13)$$

where r is the distance from the charged surface, and λ^2 is the Debye-Hückel screening length [Bard1990]. The thickness of the double layer is the distance from the charged surface to the place where $V = V_0 / 2.715$. The thickness of the double layer is calculated from the equation [Bard1990]:

$$\lambda^2 = \sqrt{\frac{4\pi N_0 k_B T}{e^2 \sum N_i Z_i^2}} \quad (3.14)$$

Where ϵ is the solvent dielectric constant, ν_0 is the vacuum permittivity, F is Faraday's constant, N_A is the concentration of ions of type i , and Z_i is the valence of anion of type i . Equation 3.11 shows that increasing the valence or the concentration of the counterions leads to compacting of the double layer. On the other hand, increasing the temperature or the solvent dielectric constant leads to an expansion of the double layer.

The interaction of two particles with identically charged double layers is described by the DLVO theory [40-50]. The theory assumes that the net force between particles is the sum of Van der Waals attraction forces and the electrostatic repulsion forces created by the interaction of the double layers. The form of the repulsion depends on the size and shape of the particle, the distance (R) between their surfaces, the double layer thickness, and the dielectric constant of the solvent. For two spherical particles of diameter a , and for hard ϵ , the potential energy of repulsion is [40-50]

$$U_R = \frac{4\pi a^2 \epsilon_0^2}{32\pi \epsilon \epsilon_0^2} \exp\left(-\frac{R}{\lambda_D}\right) \quad 3.12$$

The repulsive energy increases with increasing surface potential, solvent dielectric constant, and double layer thickness.

The total potential energy, U_T , is the sum of the attraction potential energy (from Van der Waals forces) and the repulsion potential energy:

$$U_T = U_A + U_R \quad 3.13$$

Therefore, from equations 3.7 and 3.15, the total potential energy is

$$U_2 = \frac{a_2}{2\pi b} \frac{m^2 V^2}{4kT} \exp\left(-\frac{b}{kT}\right) \quad 3.17$$

For the case of $b/a > 1$, the potential energy of repulsion becomes

$$U_2 = \frac{m^2 V^2}{b} \exp\left(-\frac{b}{kT}\right) \quad 3.18$$

Polymers Stabilization

Coagulation can be prevented by using polymers. The spatial extension of high molecular weight polymer molecules is usually comparable to or greater than the range of the Van der Waals interaction between colloids [Nag82]. Therefore, polymer molecules have the correct dimension to prevent colloid stability. There are two types of polymer stabilization: depletion stabilization and steric stabilization.

In depletion stabilization, colloidal particles are separated by free polymer chains (i.e., the polymer chains are not adsorbed on the colloid surface) [Nag82]. Depletion stabilization requires a high concentration of the polymer in the liquid. Low free polymer concentration may result in flocculation.

In steric stabilization, the macromolecules are adsorbed on the surface of the colloid. The adsorbed layer of macromolecules restrict close approach of the particles in two ways, sterically and enthalpically [Prv95]. When colloid approach each other, the entropy drops as a consequence of the overlapping of chains from

different colloid. This reduced energy results in a reduction of tension of the chain. In addition, when the polymer chain stretches, the volume around the chain is compressed, expending energy. As a result, a positive difference is created that pulls the colloid back into the space between the particles causing the particles to be pushed apart.

In order to form an effective steric barrier, certain requirements must be met [96-98]. First, the polymer chains should be strongly attached to the surface, and second, the surface of the particle should be completely covered with the polymer. In addition, the polymer chains must be long enough to keep the point of closest approach outside of the range of the attractive Van der Waals forces.

Sol-Gel Processing Route

Sol-gel processing of materials requires following certain steps. Each step can have a significant effect on the properties of the final product. These steps are hydrolysis and polycondensation, gelation, aging, drying, dehydrogenation, and annealing.

Hydrolysis and Polycondensation

Hydrolysis and polycondensation are the reactions responsible for structure evolution in sol-gel processing. Hydrolysis and polycondensation can be used for processing of inorganic, organic and polymeric sols. In order for polycondensation to occur, hydrolysis must first take place. Hydrolysis and polycondensation are opposed to both oligomer formation and cross-linking.

Hydrolysis and Condensation of Inorganic Precursors

Hydrolysis of inorganic precursors is carried out by the dissolution of salts in water. The dissolution of salts yields cations and anions. The metal cations, interact with the water by the following reaction [61-62]:



Depending on the water activity, coordination number, valency, electronegativity of the metal and pH of the solution, the following hydrolysis reaction takes place [61-62]:



where $M(OH)_n^{(n+2)}$, $M-OH$, and $M=O$, are aqua, lytrosis, and oxy-complexes respectively. The electronegativity is a measure of the atom's ability to attract electrons and it is proportional to the sum of the energy to add an electron and the energy to remove an electron from the neutral atom [61-62].

At the same pH, different complexes can result depending on the metal valence [61-62]. For a pH of 7, hydrolysis yields oxy-complexes for a metal valence above +3 and aqua-complexes for a metal valence below +3. Also, at the same valence, changing the pH results in different hydrolysis products. For example, hydrolysis of zirconia with $n = +4$ yields lytrosis, oxycomplex at low pH values (below 1.5), and aqua-complexes at high pH values.

Condensation can occur by either nucleophilic substitution or nucleophilic addition on the presence of inorganic salts. Nucleophilic substitution takes place

when the preferred coordination is satisfied [26-28]



Metathetical addition takes place when the preferred coordination is not satisfied [26-28]



Condensation by nucleophilic addition occurs when one of the reactants has a maximum coordination number (M) lower than the oxidation state (O) (i.e., one of the reactants is coordinately saturated). Except in the case of coordinately saturated precursors, it is necessary to have hydron complexes to generate condensed species. This can be accomplished by adding a base to aqua complexes or by adding an acid to aqua complexes.

Condensation can take place through either cocondensations. Coordinately saturated hydron aqua precursors undergo a nucleophilic substitution reaction to yield a hydron bridge between two metal ions. The condensation reaction is called siloxo [26-28]. Coordinately saturated metals can also undergo a nucleophilic reaction followed by water elimination to yield an oxo bridge between the metal ions. The condensation reaction is called oxidation [26-28]. For coordinately unsaturated metals, condensation takes place by nucleophilic substitution.

Hydrolysis and Depolymerisation of Metal Aluminides

Metal aluminides in general, and transition metal aluminides in particular, are very reactive species. The high reactivity is due to the presence of highly electropositive alloying groups making the metal atoms vulnerable to nucleophilic attack (like Ti and Sc in Al). The hydrolysis of metal aluminides results in the formation of hydroxides or hydrated oxides [10-12]. When limited amounts of water are added, these metal aluminides undergo partial hydrolytic reaction producing in some cases products of metal incorporation in oxide aluminides.

Group III elements are considered far less reactive than transition metal aluminides for the following reasons [10-12]:

- Transition metals are more electrophilic due to their low electronegativity. This results in the transition metals being less stable toward nucleophilic reactions such as hydrolysis and polycondensation.
- Transition metals often possess several stable coordinations, and if coordinately saturated, they are able to increase their coordination by nucleophilic reaction.

The high reactivity of most metal aluminides requires that they should be prepared with care control of reaction and other conditions of hydrolysis in order to prevent homogeneous gel. A comparison between silicon aluminides and aluminum aluminides is a good example of the effect of the electronegativity value. Silicon has an electronegativity value higher than that of aluminum [10-12]. As a result, aluminum aluminides have higher hydrolysis and condensation rates than silicon

alkalies. The difference in the hydrolysis and condensative rate between alkanol and phenol alkalies is a serious problem in the processing of phenol-formaldehyde resins.

Hydrolysis occurs by nucleophilic substitution mechanism the carboxylate-terminated strand is the source of carboxyl (Bar00). A catalyst is a base or acid that is added to influence hydrolysis and polycondensation rates and is a result of the structure of the condensed product. The water hydrolysis process depends on charge distribution in the alkoxide and the transition state. The metal cation and the leaving group have to be positively charged (Bar00). The nucleophilic substitution mechanism involves nucleophilic addition followed by proton transfer to the alkoxide or hydroxyl group within the transition state. Following that, the protonated species are removed to alcohol (Bar00).



The transient states are illustrated with a b.

Similar to the hydrolysis reaction, condensation occurs by nucleophilic substitution reactions. The condensation reaction is called amidation if the starting material is an amine.



If the condensation reaction by-product is water, then the reaction is called nucleophilic [36-38].



For coordinatively unsaturated metals, condensation occurs by cationic [36-38].



The kinetics of cation are faster than kinetics of anion and nucleophilic, since no proton transfer occurs in the formation of cation. In addition, cation has faster kinetics because $(M-O) > 0$ [36-38].

The reaction of metal chlorides, before or during hydrolysis and polycondensation, with alcohols, polyalcohols, alkoxides, and acid or base catalysts is of significant importance. Studying the reaction of these elements with metal chlorides is important to understand growth and structure evolution in the solid processes.

Metal Alkoxide Reaction with Alcohols

The type of solvent used in the sol-gel process has an important effect on reaction kinetics. Alkoxide reactivity can be modified by changing the solvent [Brd11]. The reaction of alkoxides with alcohols is called alcohol interchange reaction or alkoxide exchange which can be represented by the following equation [Brd11]



The rate with which the α -hydrox group is interchanged is a function of the size of the alkoxy group. The rate of exchange decreases from primary to secondary to tertiary groups [Brd11]. The secondary group has a higher exchangeability than the primary group, which in turn has a higher interchangeability than the tertiary group. Acetylalum is also susceptible to some factors. Bradley showed that the rate of exchange is slow in a mixture of titanium tetra-iso-butoxide and tetra-butoxide [Brd11]. On the other hand, the rate of exchange is fast in a mixture of titanium tetra-butoxide and tetra-isobutoxide. The difference in the exchange rate was attributed to steric effects.

Reaction of Metal Alkoxides with β -Diketones

β -Diketones are chemicals with molecules that have a reactive hydroxyl group. These molecules react readily with metal alkoxides through one of the following pathways [Brd11]



$\text{Mn}(\text{OAc})_5 \cdot \text{CH}_3\text{COCH}_2\text{COOAc}^2 \cdot \text{Mn}(\text{OAc})_5 \cdot \mu\text{OAc}_2\text{COOAc}^2 \cdot \text{Mn}(\text{OAc})_5$ 0.25

Acetylacetone (AcAc), hexaacetone, and ethyl acetacetone are examples of β -diketones.

β -Diketone ligands are more resistant to hydrolysis and polycondensation than alkoxide groups. They are used to block hydrolysis sites, accordingly, they are called chelating agents. Chelating agents are used to prevent precipitation of rapidly reacting alkoxides. They can also be used to specify certain functionality for the metal ions, i.e. silver coordination to some site on certain sites in order to achieve a certain structure, like the growth of one-dimensional polymers which are suitable for fiber spinning.

The addition of chelating agents has an effect on gelation time (Hei04). The gelation time increases with the increase of the amount of the chelating agent. Also, the gelation time increases with the increase of the molecular size of the chelating agent. The amount of chelating agent has an effect on particle size. Larger amounts of chelating agents result in smaller particle size due to the large number of blocked coordination sites.

Reaction of Metal Alkoxides with Alkanolamines

"Alkanolamines are derivatives of alcohols from which the hydrogen atoms of aliphatic or aromatic groups have been replaced by three amino or methyl substituted amino groups" [Bro07]. Examples of alkanolamines are ethanethiol, diethanolamine, and triethanolamine (TEA). Like β -diketones, alkanolamines are

be used as initiating agent to control the degree of hydrolysis and polymerization [Belli and Bello].

Two types of results can be produced when alkoxanes react with metal alkoxides. Some metal alkoxides show reactivity with only the hydroxyl group of the alkoxanes and simple derivatives are obtained [Bello]:



In other metal alkoxides, both the hydroxyl as well as the alkoxyl groups of the alkoxanes undergo replacement reactions with metal alkoxides to form cyclic derivatives [Bello]:



Role of Acid and Base Catalysts

Acid and base catalysts have an important role in sol-gel processing. Acid catalysts are used to enhance the process kinetics. The acid role is to protonate negatively charged alkoxide groups, eliminating the requirement for proton transfer within the reaction zone [Bello].



The ease of protonation varies for different alkoxide ligands. The hardness of protonation decreases as the electropositive power of the ligand decreases in the order, alkox, alkene, alkene, am (Bello). As a result, undissolved precipitation is

directed toward the ends of the chain. The events that take catalysis results in long polymer chains with ends branching.

The role of basic catalysts is to deprotonate the hydronium ligands (Berk).



Generally, basic catalyst enhances copolymerization kinetics. The reactivity toward methacrylate monomer is higher in the middle of the chain than at the ends. This means that acceleration is directed toward the middle rather than the ends of the chain. Consequently, more compact and highly branched species are produced.

Orbital

As time proceeds after hydrolysis and polymerization, clusters are growing either by aggregation of radicals (i.e., radical solid) or by linking polymer chains by condensation reactions (i.e., polymeric solid) (Berk). The clusters continue to grow until they collide and link together to form a single cluster. This single cluster is referred to as the gel. The gel can support stresses elastically, i.e., with no irreversible deformations (Jacobs). The time required to reach gelation point is called gelation time.

The rheological conditions of a gel initially Newtonian behavior ($\dot{\gamma} = \eta \cdot \dot{\epsilon}^{-1}$), shear thinning behavior ($\dot{\gamma} = \eta \cdot \dot{\epsilon}^{-2}$), and thixotropic behavior ($\dot{\epsilon} \cdot \dot{\epsilon}_0 = \eta \cdot \dot{\gamma}^{-1}$), where $\dot{\epsilon}$ = shear stress, η = viscosity, $\dot{\gamma}$ = shear rate, and $\dot{\epsilon}_0$ = yield stress (Jacobs). Such and were investigated the changes in viscosity as a result of viscosity changes during

spring of shear gel (Sect II). It was shown that initially, the gel exhibited Hookean behavior (the viscosity is independent of shear rate). The gel behaved this way because there was no significant particle-particle interaction due to low particle concentration.

The Hookean behavior was followed by shear thinning behavior (the viscosity decreases with the increase of the shear rate). The gel aged for a longer period of time. The behavior is due to the presence of large agglomerates that immobilize liquid resulting in high viscosity at low shear rates. At high shear rates, the agglomerates break releasing the entrapped liquid, and resulting in a decrease in the viscosity.

Further aging resulted in shear yield behavior (yield behavior with hysteresis). The long aging time results in the formation of a three-dimensional network through entanglement growth and agglomeration. A yield stress on the shear rate versus shear stress relation was observed due to the shear character of the network. After the yield stress is exceeded, shear thinning behavior accompanied by hysteresis was observed. This behavior indicates that the network structure is broken down as the shear rate is increased, but full recovery does not occur when the shear rate is decreased.

Aging

The conformation of chemical reactions after gelation is referred to as aging (West, 1990). Aging is carried out at room temperature or under hydrothermal

continues by increasing the gel in pore liquid. Aging results in strengthening, softening, and shrinkage of the network. Four processes are included in the aging process: polymerization, synthesis, softening, and phase transformation [Hsu90]. These processes can occur singly or simultaneously.

The polymerization process involves condensation reactions that increase cross-linking in the gel structure [BerkU96b].



In some gels (also, gel), polymerization continues to form other gelates due to the large concentration of silanol groups [Hsu90, 8-10]. Further hydrolysis or re-arrangement reactions can also occur during aging. The re-arrangement reaction is the reverse of the hydrolysis reaction [BerkU96].



Re-arrangement reaction can be suppressed by using excess water.

Synthesis can be defined as the shrinkage that takes place during aging as a result of condensation reactions [BerkU96]. Gel shrinkage is compensated by evaporation of pore liquid. The formation of bridging bonds by polycondensation causes synthesis [Hsu90]. As the formation of bridging bonds proceeds, the contraction of the gel increases. The synthesis mechanism in particulate gels is somewhat different than that previously described. Cohesion in particulate gels occurs as a result of the collapse of the electric double layer, and Van der Waals attraction forces resulting in synthesis [BerkU96].

Coarsening, or ripening, is a process by which dissolution and reprecipitation occur as a result of the solubility difference, K , between surfaces with different valence of curvature [Bro90]. Convex surfaces (which have positive radii of curvature) are more soluble than concave surfaces (negative radii) [Bro90, Bro92]. When a gel is immersed in a liquid in which it is soluble, dissolution occurs at the convex surfaces and reprecipitation occurs at the concave surfaces. This means that curved surfaces diffuse and adsorb gel particles. As a result of the coarsening process, small particles disappear, and small pores are filled in. Bulk growth provides the network with higher strength and stiffness.

After coarsening, the gel has a larger average porosity and a smaller surface area [Bro91]. The larger pores can result because the stiff gel produced by aging does not shrink significantly under the capillary pressure [Bro90]. The reduction in the surface area is a result of the dissolution/reprecipitation process. Coarsening does not result in shrinkage, as the centers of the particles do not move toward each other. The rate of ripening is controlled by temperature, pH, concentration, and type of solvent.

Several types of phase transformations can occur during aging. These include microphase and segregation. Microphase is a solid/liquid phase separation that occurs on a local level. This phase transformation is driven by the affinity of the polymer for itself rather than the liquid. Segregation occurs when the liquid separates into two distinct phases. For example, the presence of an unpaired metal cation in an isolated region within the pore liquid.

Crystallization is also observed in aged gels [Bir90]. Although most gels and precipitates are amorphous, aging permits the structure to rearrange by dissociation and re-precipitation, resulting in crystalline products. Crystallization can be accelerated under certain hydrothermal conditions.

Drying

Drying is the process of removing liquid such as acetone and water from the gel [Bir90]. Drying under normal conditions gives rise to capillary forces which result in shriveling of the gel [Bir90]. The resulting product is referred to as a sponge [Hewitt, Jau97]. When drying is carried out under hypercritical conditions, shriveling does not occur and the resulting gel has a high surface area. This type of gel is referred to as an aerogel [Bir90]. Only drying under normal conditions is considered in this section. Drying can be divided into three stages: constant rate stage, fine falling stage, and coarse falling stage.

Constant rate stage

In the constant rate stage, evaporation rate per unit area is independent of time. During this stage, the gel shrivels by an amount equal to the volume of liquid evaporated, and the liquid-vapor interface remains at the outer surface of the gel. As capillary forces affect the behavior of the gel during this stage, a brief discussion of relevant mechanisms follows.

If the solid-vapor interfacial energy, γ_{SV} , is higher than the liquid-vapor interfacial energy, γ_{LV} , the liquid tends to cover the solid surface and eliminate the solid vapor interface [Ra20]. The change in energy produced by spreading the liquid film is [Ra20]

$$\Delta E = \gamma_{LV} - \gamma_{SV} - \gamma_{SV}^* \quad 3.34$$

where γ_{LV}^* is the liquid-vapor interfacial energy. If $\Delta E < 0$, the liquid will spread spontaneously to reduce the energy of the system.

The condition for minimum energy can be specified using the contact angle. The contact angle, θ , is the angle between the solid surface and the tangent to the liquid surface at the contact point. The interfacial energies are related to the contact angle by the equation [Ra20]

$$\gamma_{LV} \cos \theta = \gamma_{SV} - \gamma_{SV}^* \quad 3.35$$

When $\theta > 90^\circ$, nonwetting occurs in which liquid is deposited in the capillary. When $\theta < 90^\circ$, wetting occurs and the liquid is elevated in the capillary. When $\theta = 90^\circ$, spreading occurs and the liquid covers the solid surface completely.

Liquid rises in a capillary tube to replace the solid-vapor interface with a solid-liquid interface [Ra20]. The liquid rise results in an energy gain of $2\pi rh(\gamma_{SV} - \gamma_{LV})$, where r is the tube radius and h is the height to which the liquid rises. The work done by the liquid against gravity is equal to the product of the capillary pressure, P_c , and the volume of liquid moved, $\Delta V = \pi r^2 h$. By equating the energy gained to the work done, the capillary pressure can be calculated [Ra20].

$$P_c = \frac{2\gamma_1 \cos^2 \theta_0}{\pi} = \frac{2\gamma_1 \cos^2 \theta}{\pi} \quad 3.40$$

where the negative sign indicates that the liquid is in tension.

Defining the value of tension as [Berk98]

$$\sigma = \frac{\delta}{\cos \theta} \quad 3.41$$

the capillary pressure becomes

$$P_c = -\frac{\sigma \cos \theta}{r} \quad 3.42$$

The gel network supports the tension in the liquid, and as a result, is placed in compression. Since alkoxide-crossed gels have compliant networks, the compression force causes these networks to contract into the liquid [Berk98]. Initially, the capillary pressure is low, and the value of tension is much larger than the pore radius. As drying continues, the network stiffness increases due to the formation of new bonds and the decrease in porosity. As a result of the increased stiffness of the network, the tension in the liquid rises.

The end of the constant rate stage occurs when the value of the tension becomes equal to the pore radius. This critical or "Breakthrough" point occurs when the liquid exerts the maximum force on the gel wall [Berk98; Berk99]. Past the critical point, the tension in the pore liquid cannot overcome further stiffening of the network. As a result, the network withdraws into the pores leaving modified pores near the outside surface of the gel. Therefore, during the constant rate stage, the

momentum remains at the outside surface, and the contact radius decreases correspondingly.

The first falling stage

During the first falling stage, the evaporation rate per unit area decreases with time [Bhattacharya 1996]. The second stage begins when drainage continues due to the ingress of the surface of the gel. During this stage, the liquid migrates into the exterior and outward in the transverse direction, leaving unfilled pores near the surface. However, evaporation from the outside surface continues due to the presence of a continuous liquid film that supports flow to the exterior. The presence of adjacent pathways allows flow of liquid to occur.

Liquid flow in the first falling stage is driven by a capillary pressure gradient that is a result of a vapor pressure gradient within the pores. The liquid in the transverse zone flows toward the exterior where evaporation occurs. Evaporation occurs at the outside surface because the vapor pressure is lower than it is at the inside of the pores. For a given vapor pressure, all material have the same saturation. Therefore, when gels contain variable pore sizes, larger pores empty first [Bhattacharya 1996 and Bhattacharya 2001]. If the large pores are interconnected, regions of drained pores will persist. These regions may be large enough to scatter light, resulting in an opaque gel [Bhattacharya 1996 and Bhattacharya 2001]. These opaque gels are usually clear when fully saturated or fully dried. The presence of variable pore sizes can also result in cracking during drying due to the development of differential stresses [Bhattacharya 2001].

The second filling stage

In the stage isolated liquid pockets are formed, i.e. liquid leaves the granular structure, and dries outwards by evaporation of the liquid within the body and diffusion of the vapor to the outside [26,27]. The drying front is characterized by a flow of liquid from the saturated regions which evaporates at the boundary of the unsaturated regions.

The isolated liquid pockets have a high capillary pressure, but do not exert a significant force on the solid network because they occupy a small volume fraction. As drying continues, the saturated regions withdraw into the body, which in turn expands as the total stress in the network is relieved. As a result of the network being compressed more in the saturated regions than near the drying surface, differential stress increases.

The development of a differential stress causes warping if only one side is being dried. The warping is permanent, which indicates that the unsaturated regions of the gel exhibit some plasticity during the second filling rate stage. As the saturated region thickness decreases, its contraction is more effectively prevented by the larger unsaturated regions. The resistance the saturated regions encounter to contract increases the local network tensile. This phenomenon accounts for the observed formation of cracks near the non-drying surface [26,27].

Dehydration

The dehydration process involves the removal of physically adsorbed water (physorbed water) and chemically adsorbed water (chemisorbed water) [Horn98]. Physorbed water is bound to the gel surface, while chemisorbed water is hydrogen-bonded with the gel surface. If the physorbed and chemisorbed water are not removed completely, poor optical properties or bleeding during staining can result [Horn98, Kuro98].

Thermal dehydration

In thermal dehydration, hydrogen-bonded OH groups are removed through a condensation reaction that is carried out at elevated temperatures. The rate of dehydration is a function of temperature and the concentration of remaining OH groups [Horn98]. Physorbed water is removed first at low temperatures, followed by the removal of mostly hydrogen-bonded OH groups. As the dehydration process proceeds, strongly bonded OH groups are removed, and finally, removal of adsorbed OH groups takes place. Removal of adsorbed OH groups occurs at high temperatures because diffusion of proteins is required for condensation to take place [Horn98]. For systems that suffer at low temperatures, thermal dehydration is often not sufficient to avoid bleeding, since denaturation begins before the complete removal of OH groups.

Responsive thermal dehydration can be enhanced by optimizing the gel concentration and the thermal processing conditions [Horn98]. Positive surface area,

and cavities are among the important microstructural variables that affect dehydrogenation. Dehydrogenation can be suppressed by increasing the porosity. Large pores enhance the diffusion of the condensation by product, H_2O , and temper swelling. Consequently, large pores permit complete dehydrogenation to occur before pore closure.

High surface densities are induced by selecting processing conditions that result in particulate rather than a polymeric microstructure (Berk). Particulate microstructures possess positive curvatures that facilitate dehydrogenation due to reduced hydrogen bonding. Also, the low surface area to volume ratio associated with particulate microstructures leads to faster dehydrogenation due to a reduced OH concentration on a per-gross basis. Large particles are advantageous from the stand point of surface area to volume ratio and negative radii area. Large particles have low surface area to volume ratio and low negative radii surface area. On the other hand, large particles possess smaller curvatures which can result in slower dehydrogenation.

Chemical dehydrogenation

Thermal dehydrogenation normally does not reduce the [OH] sufficiently for certain applications (i.e., optical materials) (Berk). Consequently, using another dehydrogenation technique is necessary in order to achieve low OH content. Chemical dehydrogenation has been investigated as a method to produce low OH content. This process employs the reaction between halogens and OH groups to dehydrogenate the surface.

Han et al. investigated chemical dehydrogenation of silica surface by replacing hydroxyl groups with chlorine atoms in a process referred to as chlorination [Han7]. Chlorination can be achieved by using Cl_2 gas. Chlorination using this method does not take place in temperatures $< 300^\circ\text{C}$.



3-43

Chlorination of silica gel can also be carried out by using tetravalent chlorine (NO_2Cl_2) [Bhatt7].



3-42

Although virtually complete dehydrogenation of silica surface can be produced by chlorination treatment, burning can occur when heating in the vicinity of the sulfurous acid (thiouic). This burning is a result of chlorine oxidation as it replaces the OH groups during the dehydrogenation process. Therefore, a dechlorination treatment (process to remove surface chlorine) is necessary to prevent burning. In regards of incomplete chlorination, Cl may be removed by the following reaction [Saito6].



3-43

Dechlorination can be carried out by heating below the melting temperature in dry oxygen environment [Saito6]. The oxidation reaction is diffusion controlled, and the result is a significant decrease in chlorine.

Since the chlorine content is proportional to the surface area of the gel, reduction of surface area prior to the chlorination treatment can result in a lower

reduced chlorine content [BaskI]. Gels can be pre-sintered in order to reduce surface area. The degree of pre-sintering is controlled so that no closed pores are developed. The development of closed pores hinders the sintering process.

Fluorine can also be eliminated by using fluorine instead of chlorine [BaskI]. Fluorine can be introduced in HF, NH_4F , or SiF_4 , and can replace ClH groups in a manner similar to Cl [BaskI].



3-44

Fluorine does not occur when using fluorine due to stronger Si-F bond. However, fluorine is retained in the final gel.

Substrates:

Sintering is a densification process that is driven by the tendency to decrease the surface area in order to reduce the surface free energy of the material [BaskI and BaskII]. The surface free energy is reduced by the elimination of the initial vapor surface. Gels generally have large surface areas, resulting in a relatively high driving force for sintering. The high driving force produces sintering at exceptionally low temperatures, where the transport processes are slow. Amorphous materials sinter by viscous flow, while crystalline materials sinter by sub-lattice diffusion [BaskII]. One of the important aspects in sintering and substrate sintering is the effect of surface curvature on vapor pressure into the surface. The vapor pressure difference has an important role in the material transfer during sintering.

The pressure difference across a curved surface can be determined by considering a bubble being drawn on a liquid bath by a capillary [Kro76]. If the gravitational effect is negligible, the only resistance to expansion of the bubble is the increased surface energy due to the increase in the surface area. During equilibrium, the following equation must hold [Kro76]

$$\Delta P = \gamma \left(\frac{1}{r_1} + \frac{1}{r_2} \right) \quad 3-45$$

where ΔP = the pressure difference across the curved surface, γ = surface per unit area. The left hand side of the equation 3-45 represents the work of expansion, and the right hand side represents the increased surface energy. The values of $d\sigma$ and dA , with respect to the radius of curvature, r , are [Kro76]

$$d\sigma = \gamma \left(\frac{1}{r_1} + \frac{1}{r_2} \right) \quad 3-46$$

$$dA = 2\pi r dr \quad 3-47$$

Substituting the values of $d\sigma$ and dA in equation 3-45 results

$$\Delta P = \gamma \left(\frac{1}{r_1} + \frac{1}{r_2} \right) \quad 3-48$$

Equation 3-48 is valid for spherical shapes. For more general shapes [Kro76]

$$\Delta P = \gamma \left(\frac{1}{r_1} + \frac{1}{r_2} \right) \quad 3-49$$

where r_1 and r_2 are the principal radii of curvature

The increase in vapor pressure due to an applied pressure of ΔP can be calculated from [Kro76]

$$\frac{RT - RT_0}{P_0} = \frac{RT_0}{P_0} \left(\frac{1}{T_0} - \frac{1}{T} \right) \quad 3.50$$

where V = molar volume, p = vapor pressure over the curved surface, p_0 = vapor pressure over a flat surface, and T = gas temperature. Rearranging equation 3.50

$$\ln \frac{P}{P_0} = \frac{RT_0}{p_0 V} \left(\frac{1}{T_0} - \frac{1}{T} \right) \quad 3.51$$

where M = molecular weight, ρ = density, and T = temperature. Equation 3.51 relates the difference in the vapor pressure to the curvature, and is called the Raoult-Prandtl (Raftree) equation.

Motion of a single spherical particle

The driving force for viscous smearing is a lowering of the surface energy by reducing the surface area. Considering the enthalpy of a pair of spheres, Prandtl derived a model for viscous smearing [Raftree and Brattell]. When two spherical particles are in contact, there is a negative pressure at the small negative values of curvature of the contact area (δ) compared to the surface of the particle. The pressure difference causes a viscous flow of material to the neck region.

During viscous flow smearing, the neck width and the contact of the particles approach one another causing shrinkage. The rate of growth of the neck area was illustrated by Prandtl [Raftree, Raftree, Raftree and Brattell].

$$\frac{dA}{dt} = \left(\frac{2T_{00}}{3\mu_0} \right)^{\frac{1}{2}} \frac{1}{4} \quad 3.52$$

where r_s = neck radius, r_p = particle radius, γ_{sv} = solid/vapor interfacial energy, η = viscosity, and t = time. The relation was verified experimentally by Kawaguchi, Kligler, and Sung (Kawaguchi and Kligler). The increase in the neck diameter is proportional to the square root of time. The rate determining factors for this process are surface tension, viscosity and particle radius. Higher scattering rates are achieved when the particle size and viscosity are small and surface tension is large.

The processing temperature has an important effect on the scattering rate. The scattering rate is proportional to η_p/r_p . A change in the temperature results in changes in the nature of the surface OH groups, and consequently, in the surface energy [Berk]. However, the loss of OH occurs over a wide range of temperatures. Over the same range of temperatures, the viscosity changes by many orders of magnitude. As a result, the temperature dependence of the scattering rate is governed entirely by the viscosity [Berk].

At low temperatures, the viscosity of glasses is governed by [Zerk]

$$\eta = \eta_0 \exp \left(\frac{\Delta G}{kT} \right) \quad 3.10$$

where ΔG = activation energy for viscous flow, k = Boltzmann's constant, T = temperature, and η_0 can be calculated from [Zerk]

$$\eta_0 = \frac{kT}{\tau V_m} \quad 3.11$$

where τ is a frequency factor, and V_m is the volume occupied by a molecule. Equation 3.11 leads to an Arrhenius dependence for the viscosity [Zerk].

$$\log \eta = A + \frac{B}{T} \quad (3.53)$$

where A and B are constants.

At high temperatures, the viscosity of glass departs from Arrhenius behavior to follow what is called Vogel-Politzer-Thomson empirical equation (Zerilli, 1976)

$$\log \eta = A_1 + \frac{B_1}{T - T_1} \quad (3.54)$$

where A₁, B₁, and T₁ are constants.

Kengay and Flory developed a procedure to derive the shrinkage rate (Kengay, 1962). Considering the volume of the melt region (Kengay)

$$V_m = \frac{\pi R_m^3}{3} \quad (3.55)$$

Substituting equation 3.52 or 3.57 results in

$$\dot{V}_m = \frac{\partial \log \eta^{-1}}{\partial \eta} \quad (3.56)$$

Taking the derivative of V_m with respect to η

$$\frac{dV_m}{d\eta} = \frac{16\pi R_m^2}{45} \quad (3.57)$$

where the negative sign indicates the decrease in volume. The volume decrease of the sphere at each instant is (Kengay)

$$\frac{dV_m}{V_m d\eta} = - \frac{16\pi R_m^2}{45 \eta^2} \quad (3.58)$$

where V_0 is the initial volume of the sphere. Considering each sphere has a number of contacts $n = n_0$ and by integrating equation 3-61 [Bhattacharya 1998]

$$\frac{\Delta F_{\text{min}}}{V_0} = \frac{2\pi\gamma h^2}{3n^2g^2} \quad (3-62)$$

Equation 3-62 represents the shrinkage rate during viscous flow sintering. The expression is expected to lead to a volume shrinkage of 2% with reasonable precision.

Shrinking of crystalline materials

As with viscous flow sintering of amorphous materials, sintering of crystalline materials is driven by the tendency to lower the surface free energy by reducing the surface area [Bhattacharya 1998 and Bhattacharya 2004]. The surface free-energy is reduced by replacing the high-energy solid-vapor surface by a lower-energy solid-solid surface. Material transfer during sintering of crystalline materials is influenced by the pressure difference and changes in free energy across a curved surface.

Evaporation-condensation and solid-state diffusion are the mechanisms by which material can be transferred in a crystalline material. Evaporation-condensation and solid-state diffusion paths are illustrated in Figure 3-5. Material transport by solid-state diffusion is divided into the following mechanisms [Bhattacharya, 2004]

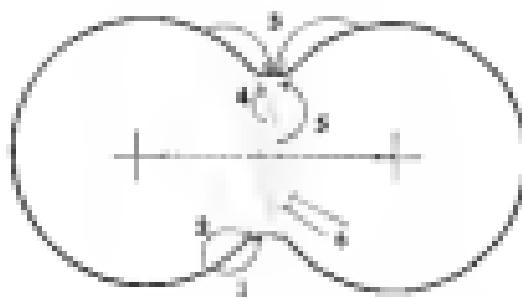


Figure 3-1. Water transport paths during mid-season maturing. 1) Boundary diffusion; 2) Lumen diffusion from the surface; 3) Trigone transport; 4) Boundary diffusion; 5) Lumen diffusion from the pericarp (mesocarp); and 6) Lumen diffusion from the bulk. Adapted from [Kut79].

- Surface diffusion: in which the surface is the source and the path of the transported material.
- Lattice diffusion: in which the surface, grain boundary, or dislocation is the source and the surface is the path
- Grain boundary diffusion: in which the grain boundary is the source and the path of the transported material

Evaporation-condensation mechanism:

In the evaporation-condensation mechanism, material is transported from the region of high vapor pressure (the particle surface) to the region of low pressure (the void). The evaporation-condensation process results in a decrease in the energy of the system, but it does not produce densification [Kro86]. Changes in pore-shape are produced during this process, but shrinkage does not occur.

In order to determine the growth rate of the neck between two particles, consider the Thoenen-Prony-Li equation for two bonded particles [Kro86, Kro97]

$$\frac{p_1 - p_2}{p_1} = \frac{2M_1 A_1 - A_2}{\rho R^2 A_2 - A_1} \quad (4.12)$$

where p_1 is the pressure over the small neck of curvature of the neck. The pressure difference $p_1 - p_2$ is used, and $A_2 > > A_1$. As a result, to a good approximation, is $p_1/A_1 \approx \Delta p/A_2$, and equation 4.12 becomes [Kro97]

$$\Delta p = \frac{RT^2}{2\pi d^3} \quad (3.62)$$

where Δp is the difference between the vapor pressure of the small, negative value of curvature and the vapor pressure over the nearly flat particle surface.

Using the Langmuir equation for the rate of material transfer, in (3.60):

$$m = a k T \left(\frac{M}{2\pi R^2} \right)^{1/2} \quad (3.63)$$

where a is an accommodation coefficient that is approximately equal to 1. The rate of condensation is equal to the volume increase (3.62):

$$\frac{dV_{\text{cond}}}{dt} = \frac{2}{3} \frac{\Delta p}{R} \quad (3.64)$$

From the geometry of the two spheres in contact, Figure 3.3, $a = r_1^2/2r$, $A = \pi r_1^2/2r$, and $V = \pi r_1^3/3r$. Substituting values for m , A , and V in equations 3.63 and integrating, the relationship for the rate of growth of the bond area between particles is obtained (Bard, 1976; Kau76):

$$\frac{dA_{\text{cond}}}{dt} = \frac{2\sqrt{2\pi} r_1^{1/2} m}{3} \left(\frac{1}{R} - \frac{1}{r_1} \right) \quad (3.65)$$

In addition to time, the main variables that affect the rate of particle coagulation through this process are the particle radius and the vapor pressure. The vapor pressure increases exponentially with temperature, resulting in a strong dependency of evaporation-condensation process on temperature (Kau76).

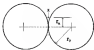


Figure 3-2. Schematic of the initial stages of clustering by evaporation/condensation mechanism. Adapted from [Koch].

Solid state migration

The difference in the free energy between the neck area and the surface of the particle provides the driving force for material transfer [Ko79]. Matter can move from the surface, from the grain boundary, or from the bulk by surface, grain boundary, or lattice diffusion. Similar to evaporation-condensation, the transfer of material from the surface to the neck by surface or lattice diffusion does not lead to shrinkage or densification [Br84] and [Br74]. Shrinkage and densification take place when material is transported from the particle volume or from the grain boundary between particles.

Considering the case of matter transport from the grain boundary to the neck by lattice diffusion, and from the geometry of the neck region as shown in Figure 3.3, the following is obtained [Ko79]:

$$\mu = r_g^3/6\pi, V = \pi r_g^2/2r \quad 3.67$$

The surface energy problem as a case of vacancies in the regions of negative curvature [Br84]. This excess of vacancies results in a flux of vacancies away from the perimeter of the neck. The vacancy flux per unit time per unit length, J , can be written as follows [Ko79]:

$$J = Dv \Delta M \quad 3.68$$

where Dv = vacancy diffusion coefficient, ΔM = the excess concentration of vacancies. The excess concentration of vacancies is determined from [Ko79]:

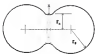


Figure 3-3 Schematic of one type of solid-state snowplow. Adapted from [Kato].

$$\frac{dN}{dt} = \frac{m^2 N^2}{4\pi R} \quad (3.6)$$

where a = atomic radius, and N_0 = density of atoms in a plane system. The self-diffusion coefficient is related by [Kad55]:

$$D_1 = m^2 D_2 N_0 \quad (3.7)$$

Also, the rate of volume change, dV/dt , is related to the density current, J_1 by [Kad55]

$$\frac{dV}{dt} = -2\pi a^2 J_1 \quad (3.8)$$

Substituting equations 3.69, 3.70, and 3.71 into equation 3.68 and integrating yields the neck growth rate [Kad55]:

$$\frac{r_{\text{neck}}}{r_0} = \left(\frac{4\pi m^2 D_1}{3\pi} \right)^{1/2} \left(\frac{J_1}{J_0} \right)^{1/2} \quad (3.9)$$

The shrinking rate is determined through the same procedure that was used for nucleus merging [Kad55]

$$F_1 = \frac{a}{3} \left(\frac{4\pi m^2 D_1}{3\pi} \right)^{1/2} \left(\frac{J_1}{J_0} \right)^{1/2} \quad (3.10)$$

and

$$\frac{dV}{dt} = \frac{J_1}{3} \left(\frac{4\pi m^2 D_1}{3\pi} \right)^{1/2} \quad (3.11)$$

Equation 3.11 is expected to hold to a volume shrinking of 2%

Equations 3.23 and 3.24 indicate that the neck growth rate is proportional to $t^{1/2}$, and that the shrinkage rate is proportional to $t^{1/3}$ (Kaz96). Control of particle size is important, since the shrinking rate is roughly proportional to the square of the particle radius. This means that as the particle size is increased, the shrinking rate is decreased.

The mobility of atoms is high within the grain boundary. Consequently, diffusion in the grain boundary is rapid. However, the flux of diffusing atoms is small because the grain boundary cross-sectional area is very small (Bv94). Diffusion through the lattice, on the other hand, is very slow, but the flux can pass through a larger area. As a result, the net rate of transport by lattice diffusion may be greater than that of grain boundary diffusion.

The particle size can determine which transport mechanism is dominant. Grain boundary diffusion is dominant in case of small grains due to the large volume fraction occupied by the grain boundary. The activation energy for lattice diffusion is higher than that of grain boundary diffusion (Juli91). However, the lattice diffusion coefficient increases rapidly with temperature. As a result, lattice diffusion becomes more important at high temperatures. It has been observed that surface diffusion is most important during the early stages of sintering. The diffusion affects the neck diameter but not the shrinkage or porosity (Kaz96). Grain boundary and lattice diffusion become important following the early stages of sintering.

As shown in equations 3.11 and 3.24, the sintering rate is proportional to t^2 for viscous sintering, and is proportional to $t^{1/2}$ for lattice or volume diffusion. This

means that viscous flow settling is much faster than solid-state diffusion settling. The difference in the沉降 rate for the two mechanisms can have significant effects on the densification behavior of these systems. Saito and Park reported very rapid densification in aluminosilicates with compositions that contained large amounts of liquid phase [20-22]. High densification rates persisted up to an aluminum content of 74 wt%, at which a sharp decrease in the densification rate was observed. This sharp decrease in densification rate occurred at the transition from multistable region to a stable phases region. This transition was associated with the elimination of the glassy phase. The drop in the densification rate was attributed to absence of viscous settling and the occurrence of solid-state settling.

CHAPTER 4 COMPOSITE MATERIALS

Definitions and Characteristics

Composites are materials that consist of two or more chemically and physically distinct constituents on a microscopic level [Agr00, Hol01]. Composites can be made by mixing the separate constituents in such a way that the properties of one constituent in the other can be done in a controlled way to improve properties. Since the constituents may be individually tailored to enhance separate physical or chemical characteristics, the properties of the composite should be superior to those of the individual constituents. Composites consist of one or more discontinuous phases, called the reinforcing material, embedded in a continuous phase, called the matrix. In general, reinforcing materials are stronger and harder than the matrix.

Properties of composites are highly dependent on the properties of their constituent materials. The properties of composites are also influenced by the distribution of the constituents and the interaction among them [Agr01]. These properties may be the volume fraction sum of the properties of the constituents, as the properties of the composite work together to provide properties that are not accounted for by the volume fraction sum of the constituents properties. Composites can be described by the geometry of the reinforcement. The geometry of the reinforcement is described by size, shape, and size distribution. Composites with

Identical reinforcement quantity may differ in concentration, concentration distribution, and orientation.

Concentration is considered the most important parameter influencing the composite properties [Aguilera]. It is considered as unavoidable and不可避諱的 to discuss the properties of the composite. The concentration distribution can be used to determine the homogeneity of the composite material system [Aguilera]. Particles may be uniformly dispersed in a composite without touching each other. Particles can also be arranged in a way to form a network with a continuous path connecting all particles.

The orientation of the reinforcement has a great influence on the isotropy of the system [Aguilera]. In the case of spherical reinforcement particles, the composite behaves as an isotropic material. For reinforcement particles with unequal dimensions, isotropy is obtained if they are randomly oriented, as example is the randomly oriented, short-fiber reinforced composite. In some cases, anisotropy is desired in order to impress a certain property on a specific direction. Continuous-fiber-reinforced composites can be anisotropic, if the fibers are aligned in one direction or worse in stacked plies. Anisotropy can also be introduced by using certain manufacturing processes, such as extrusion of short-fiber composites.

The majority of structural composites have been fibrous to improve the mechanical properties, such as strength, toughness, stiffness, and high-temperature performance [Aguilera]. The property of the reinforcement has a strong influence on the strength/elastic modulus. Consequently, reinforcement phase porosity can be

considered as a basis for classification of composites. Composites can be divided into two major categories [Agar0]. The first category is called particle-reinforced composite (particle composite). This category includes all composites with particles that are *irregular* in nature. The particles may be spherical, plate-shaped, cubic, tetragonal, or any other regular or irregular shape that is approximately equiaxed. The second category consists of fiber reinforced composites (fibrous composites). A fiber is distinguished by its length being much greater than its transverse dimensions [Agar0]. The emphasis in this study is on unidirectional fiber composites, other composites are beyond the scope of this study.

Unidirectional Fiber Composites

Unidirectional fiber composites consist fibers that are aligned parallel to each other in a single direction. These composites have transverse isotropy; their high strength to weight ratio, and controlled anisotropy [Agar0]. Unidirectional fiber composites are divided into discontinuous (fiber) fiber reinforced composites and continuous-fiber unidirectional composites. In discontinuous-fiber unidirectional composites the fiber orientation cannot be controlled easily. In these composites the load bearing capability is a function of the fiber length.

Continuous-fiber composites have a higher strength and modulus values in the direction of the fiber axis than the strength and modulus of short-fiber composites [Agar0]. However, these composites are very weak in the transverse direction.

Therefore, continuous-fiber composites are superior to short-fiber composites when load is applied in the longitudinal direction (parallel to fibers).

The use of fibers in high performance engineering materials is based on the following characteristics (Chart):

- A high aspect ratio (length (L)/diameter (d)) that facilitates the transfer of a major part of the applied load by the matrix or strong fibers
- A small fiber diameter with respect to grain size. This allows a higher fraction of the theoretical strength to be attained than that possible in a bulk form, because the smaller size has a lower probability of having large surface flaws.
- A high degree of flexibility that is a characteristic of a material with high modulus and small diameter. The flexibility allows a variety of techniques to be used in manufacturing composites with these fibers.

Unidirectional composites consist of parallel short or continuous fibers embedded in a matrix. Several unidirectional layers (each referred to as a lamina) can be in a specified orientation, to form a laminate [Pugh83, Agar90]. Figure 4.1 shows a continuous-fiber composite lamina. Laminae are considered building blocks that are used to make high-performance structural elements. Since the main application of unidirectional composites is for load bearing, understanding the mechanics of these composites is essential.

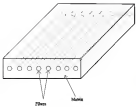


Figure 4-1: Unidirectional woven/roff composite lamina. Adapted from Agapiou.

Mechanics of Fiber Composites

Designing composites to sustain high loads for various applications requires a thorough understanding of composite mechanics. The behavior of unidirectional composites is a result of the behavior of the interface between the fiber and the matrix, and the behavior of the fiber and the matrix themselves [Choi7].

The fiber interface is responsible for transmitting the load from the matrix to the fiber [Agab]. The fibers contribute the greater portion of the composite strength. This means that the efficiency of load transmission from the matrix to the fibers can have a large influence on the strength of the composite. There are two types of bonding that can exist at the fiber-matrix interface, mechanical bonding and chemical bonding [Choi7]. Mechanical bonding can occur by simple mechanical keying effects between two surfaces. It can also be produced by the constraint of the matrix against the fibers. In most cases, mechanical bonding alone is not enough to form an effective reinforcement. However mechanical bonding can add to the overall bonding, or the presence of reactive bonding.

Chemical bonding can be divided into two types, dissolution and wetting bonding, and reactive bonding [Choi7]. In dissolution and wetting bonding, interaction between components occurs at an electronic scale. The bond strength varies from weak Van der Waals to strong covalent bonds. Intimate contact is required between the fiber and the matrix to achieve the kind of bonding, along

these interactions are short range. This implies that no contaminants on the fiber surface, or entrapped air or gas bubbles at the interface, should be allowed to exist.

Reaction bonding occurs by transfer of atoms from the fiber and the matrix to the interface, which is controlled by the reaction rate (Eshelby). The reaction products and the reaction rates depend on the matrix composition, reactor size, and temperature. The thickness of the surface reaction zone (x) is generally described by the formula [Ochi77]

$$x = \sqrt{Dt} \quad 4.1$$

where D = diffusion coefficient, t = time. The diffusion coefficient is determined by the formula [Ochi77]

$$D = D_0 \exp(-\frac{Q}{kT}) \quad 4.2$$

where D_0 = constant, Q = activation energy, k = Boltzmann constant, and T = temperature.

Modeling of Unidirectional Composite Fiber Composites

Consider the case of a continuous-fiber composite with parallel fibers under a longitudinal tensile load. Assuming a perfect fiber to matrix bonding, the longitudinal strains in fibers (ϵ_f), matrix (ϵ_m), and composite (ϵ_c) are equal [Agarwall and Mukherjee]

$$\sigma_y = \sigma_x \cdot \frac{E_f}{E_m} \quad (4.5)$$

From linear elasticity theory, the stress and the strain are proportional to each other according to Hooke's law (Eq. 2.6):

$$\sigma = E \epsilon \quad (4.6)$$

where σ is the stress, which is the amount of load applied per unit area, and E is Young's elastic modulus. Assuming both fibers and matrix behave as linearly elastic materials [Meh88]

$$\sigma_y = E_f \epsilon_y = E_m \epsilon_m \quad (4.7)$$

$$\sigma_y = E_f \epsilon_y = E_m \epsilon_m \quad (4.7)$$

where ϵ_y = fiber strain, ϵ_m = matrix strain, E_f = fiber elastic modulus, and E_m = matrix elastic modulus.

The tensile load applied on the fibers, P_f , is shared by the matrix and the fibers [Meh88].

$$P_f = P_f / P_m \quad (4.7)$$

where P_f = load applied on fibers, and P_m = load applied on matrix. Using the definition of strain, equation 4.7 becomes [Ngoh01 and Meh88]

$$\sigma_y = \sigma_f \frac{A_f}{A_m} = \sigma_m \frac{A_m}{A_f} \quad (4.8)$$

where σ_y = average tensile stress in the composite, A_f = net cross-sectional area for fibers, A_m = net cross-sectional area for matrix, A_f = cross-sectional area of the

composite, i.e. $E_c = E_f + E_m$. Defining fiber and matrix volume fractions (Agard and Muhl) and ρ :

$$E_c = \frac{E_f}{V_f} + \frac{E_m}{V_m} \quad 4.10$$

$$E_c = \frac{E_f}{\rho_f} + \frac{E_m}{\rho_m} \quad 4.11$$

This equation 4.11 becomes (Agard):

$$E_c = \rho_f E_f + \rho_m E_m \quad 4.11$$

or

$$\rho_f = \frac{E_c - E_m}{E_f - E_m} \quad 4.12$$

Dividing equation 4.11 by the stress yields (Muhl):

$$E_c = E_f V_f + E_m (1 - V_f) \quad 4.13$$

where E_c = average composite elastic modulus. Equations 4.12 and 4.13 indicate that the contributions of the fibers and the matrix to the average properties of the composite are proportional to their volume fraction. Such a relationship is referred to as the rule of mixture (Agard and Muhl).

The fraction of load carried by the fibers in a unidirectional composite fiber layout can be determined by dividing the load applied to the fibers by the load applied to the composite (Muhl):

$$\frac{F_f}{F_m} = \frac{1}{1 + \frac{E_f}{E_m} \left(\frac{1}{V_f} - 1 \right)} \quad 4.10$$

Equation 4.10 indicates that in order to attain high stresses in the fibers and thereby use the fibers efficiently, it is necessary for the fiber modulus to be much greater than the matrix modulus [Aguiar]. Figure 4.3 shows the fraction of the composite load carried by the fibers. As shown in the figure, the fraction of the total load carried by the fibers increases with the increase in ratio of fiber modulus to matrix modulus and the increase in the volume fraction of fibers. However, when fiber volume fraction exceeds 80%, properties start deteriorating due to the inability of the matrix to sufficient the bonding of fibers, resulting in poor fiber matrix bonding and void formation in the composite.

Fiber failure strain is generally lower than the matrix failure strain [Mallik]. The tensile rupture of fibers will result in a tensile rupture in the composite. From equation 4.10, the longitudinal tensile strength of a unidirectional continuous fiber composite can be calculated as [Aguiar, Holtz, 1992]

$$\sigma_{\text{lf}} = \sigma_f V_f / (V_f \sigma_m (1 - V_f)) \quad 4.11$$

where σ_{lf} = the longitudinal tensile strength of the composite, σ_f = fiber tensile strength, and $(V_f \sigma_m)$ = matrix stress at the fiber failure stress. The strengthening

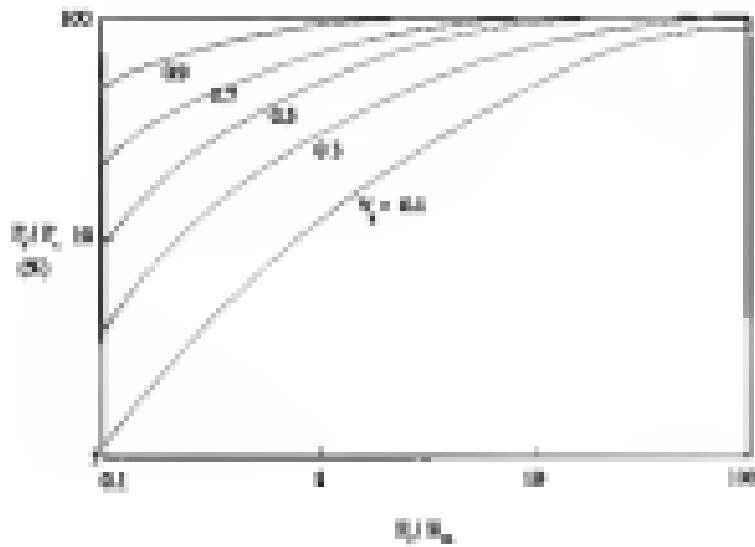


Figure 4.3. Fraction of composite load carried by fibers as a function of fiber modulus/modulus ratio for different fiber volume fractions. Adapted from (Maddams, 1991).

efficiency is not achieved unless the strength of the composite exceeds that of the matrix alone [Aguiar]

$$\sigma_{\text{eff}} = \sigma_m F_f + (\sigma_m \lambda_f) (1 - F_f) \sigma_m \quad 4.16$$

where σ_m = the strength of the matrix. Using equation 4.16, a critical volume fraction of fibers, V_{cr} is defined [Aguiar and Malhi]:

$$F_f = \frac{\sigma_{\text{eff}} - (\sigma_m \lambda_f)}{\sigma_m - (\sigma_m \lambda_f)} \quad 4.17$$

This critical volume fraction of fibers has to be exceeded in order for strengthening to occur.

Mechanics of Discontinuous, Parallel Fiber Composites

When a load is applied to a discontinuous fiber bundle, it is transferred to the fibers by shear stresses acting at the fiber/matrix interface [Malhi]. The lower modulus for the matrix results in the longitudinal strain in the matrix being higher than that in aligned fibers. As a result, a shear stress distribution across the fiber/matrix interface is established, if perfect-fiber matrix bonding is assumed.

The normal stress distribution in a discontinuous fiber can be calculated by equilibrium analysis. Considering an element with length dx , at a distance, x , from a fiber end (as shown in Figure 4.18), the force equilibrium equation for dx is [Malhi]

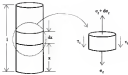


Figure 4-3 Longitudinal tensile loading of a discontinuous fiber in a unidirectional composite. Adapted from [Jia2003].

$$\left(\frac{3}{4} \sigma_0^2 (2\pi r_0)^{1/2} \right) = \left(\frac{3}{4} \sigma_0^2 r_0^2 \right) \text{radius}_0, \quad 4.22$$

where r_0 = longitudinal stress in the fiber at a distance r from one of its ends, σ_0 = shear stress at fiber-matrix interface, d_0 = fiber diameter. Equation 4.22 can be simplified to [Mehlitz]

$$\frac{dr_0}{dr} = \frac{4r_0}{d_0}, \quad 4.23$$

Ignoring the shear transfer at the fiber ends, and assuming the axial shear stress is constant and equal to the matrix yield shear stress, integration of Equation 4.23 yields [Mehlitz]

$$r_0 = \frac{4r_0}{d_0} \ln \frac{r}{r_0}, \quad 4.24$$

Equation 4.24 indicates that the fiber stress is not uniform. The fiber stress is zero at the ends and increases linearly to the maximum value at the central portion of the fiber. For short fibers, the maximum fiber stress occurs at $r = R/2$, that [Agard and Mehlitz].

$$\sigma_{f0} = \sigma_0 \frac{R}{d_0}, \quad 4.25$$

"The minimum fiber length in which the maximum fiber stress can be achieved" is referred to as load-transfer length (L_0) [Agard]. The load is transferred from the matrix to the fiber over the load-transfer length, which is given by [Agard]

$$\frac{L_0}{d_0} = \frac{2r_0}{\sigma_0}, \quad 4.26$$

Since σ_{f0} is dependent on the applied stress, the load-transfer length is also dependent on the applied stress. A critical fiber length (L_0) can be defined as the

minimum fiber length at which the fiber strength (σ_{sf}) can be achieved [Agui00,Mat00].

$$\frac{L_c - L_0}{d} \geq \frac{2\sigma_{sf}}{3\sigma_s} \quad 4.23$$

The critical fiber length is independent of applied stress. The maximum value for the load-carrying length is the critical length.

Figure 4-4 shows the significance of the critical fiber length to the longitudinal stresses of the fiber. In the case of fiber length smaller than the critical length, the maximum fiber stress may never reach the value for fiber strength [Mat00]. As a result, either the stress on the fiber's main material bond may fail before fibers reach their potential strength. In the case of fiber length equal to the critical length, the maximum fiber stress reaches the fiber strength at the middle of the fiber. The last case is when the fiber length is greater than the critical length the maximum fiber stress may reach the fiber strength over much of its length. However, the fiber cannot ineffective over a distance equal to $L_c/2$ from each end. For effective strengthening, the selected fiber length should be much greater than the critical length.

The average fiber stress can be calculated from the formula [Agui00 and Mat00]

$$\sigma_{av} = \frac{1}{L_c} \int_{L_0}^{L_c} \sigma_s ds \quad 4.24$$

The quantity represented by the integral is the area under the curve of fiber stress

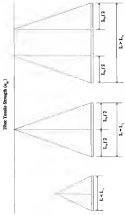


Figure 4: Relationship of vertical line lengths to the length of parallel sides of a trapezoid (see [Mak1]).

matrix length (Figure 4.3). Therefore, the average fiber stress is [Maddi, Agarwal]

$$\sigma_{\text{av}} = \sigma_{\text{fc}} \left(1 - \frac{L}{L_0}\right) \quad 4.25$$

In the case of $L > L_0$, equation 4.25 becomes:

$$\sigma_{\text{av}} = \sigma_{\text{fc}} \left(1 - \frac{L_0}{L}\right) \quad 4.26$$

and in the case of $L < L_0$, equation 4.25 becomes:

$$\sigma_{\text{av}} = \frac{\sigma_{\text{fc}}}{3} \quad 4.27$$

For $L > L_0$, the longitudinal tensile strength of the composite is determined by substituting $L_0 = L_1$ and $\sigma_{\text{fc}} = \sigma_{\text{fc1}}$ and using the following rule of mixture (Maddi):

$$\sigma_{\text{av}} = \sigma_{\text{fc}} \sigma_{\text{m}} F_1 \sigma_{\text{m}} F_2 \quad 4.28$$

Thus, the longitudinal tensile strength of a unidirectional discontinuous fiber composite is [Agarwal, Hellmich, and Maddi]

$$\sigma_{\text{av}} = \sigma_{\text{fc}} \left(1 - \frac{L_0}{L}\right) F_1 \sigma_{\text{m}} F_2 \left(1 - \frac{L_0}{L}\right) \quad 4.29$$

For the case of $L_0 > L_0$, equation 4.29 becomes identical to equation 4.15, which is used for continuous fibers. A comparison between equation 4.15 and equation 4.29 shows that continuous fibers always show more strength than a matrix more effectively than short fibers.

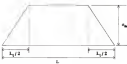


Figure 4-3. Longitudinal stress distribution along a discontinuous fiber under impact load testing [44,68].

In the case of $L < L_p$, no fiber failure occurs. Instead, failure occurs by one of the following failure modes [Mai94]

– Fiber matrix traction bond failure followed by fiber pullout. In this case, the longitudinal tensile strength of the composite is [Mai94]

$$\sigma_u = \sigma_m \frac{L}{L_p} (1 - \sigma_m (1 - \rho)) \quad (4.20)$$

where σ_m = shear strength of fiber-matrix interface, σ_{m0} = tensile stress at the instant of fiber pullout.

– Matrix failure, in which the longitudinal tensile strength of the composite is [Mai94]

$$\sigma_u = \sigma_m \frac{L}{L_p} (1 - \sigma_m (1 - \rho)) \quad (4.21)$$

where σ_{m0} = tensile strength of the matrix. Which mode is responsible for the failure is dependent on the relative values of σ_m and σ_{m0} .

The discontinuities caused by the presence of fiber ends result in stress concentrations. The stress concentrations are produced because the load that is not carried by the fiber due to the discontinuity must be carried by other fibers. These stress concentrations can have detrimental effect on the strength of the composite.

Failure of Underloaded Composite Under Longitudinal Tensile Load

Failure of underloaded composites that are subjected to longitudinal tensile load is initiated by fiber breaking [Ngai98]. Fiber strength in reality is not a single value [Mai94]. Fiber strength follows a statistical distribution due to the presence of defects. Consequently, it is expected that a few fibers will fail at stress levels

below the average strength. The remaining fibers will carry higher stresses, and may fail simultaneously.

The stress distribution in a fiber changes after breaking occurs. The stress at each of the broken ends becomes zero [Mat88]. However, the stress builds back up to reach the average value over a distance of $1/\beta$ from each end. The stress states in the regions of the broken ends contain the following [Mat88]:

- high shear stress concentrations in the matrix within the fiber end regions,
- stress concentrations at the well-cracked open boundary of the fiber, and
- an increase in the normal stress in the neighboring fibers.

The presence of these stresses can result in failure of the composite.

Failure Processes

Fracture toughness of a unidirectional composite is the sum of the energies consumed by several failure processes. These failure processes are fiber debonding, fiber pullout, fiber fracture, and matrix cracking or yielding. [Mat88]. An advancing crack always has a longitudinal stress concentration at its tip. The stress component perpendicular to the longitudinal stress and the shear stress component may reach high values slightly ahead of the crack tip. Depending on the strength of the fiber-matrix interface, these stress components can cause debonding of the fibers from the surrounding matrix by breaking the chemical and secondary bonds between the fibers and the matrix [Aga88, Mat88]. Fiber debonding is more probable to occur than fiber pullout failure when the interfacial bonding is weak and fiber strength is high.

A debonding crack may run at the interface or in the adjacent matrix depending on their cohesive strength. In both cases, a new surface is created, which results in an increase in the fracture energy.

When a load is applied, fiber-matrix bonding resistance is varied because due to the statistical distribution of surface flaws [Maddi]. The opening of the matrix crack causes broken fibers to pull out from the surrounding matrix earlier than fibers breaking again in the plane of composite fracture [Agapi, Maddi]. Fiber pullout occurs when brittle or ductile matrix fibers are used to reinforce a tough matrix. Fiber pullout occurs in the case of fibers whose ends are within a distance of $L_p/2$ of the composite fracture surface. Fiber pullout is opposed by friction at the fiber-matrix interface which results in an increase in the fracture energy. For cases when the fiber length for broken fiber (length) is greater than $L_p/2$ or the overload strength is high, fiber failure or fiber debonding occurs first followed by fiber pullout.

The difference between fiber pullout and fiber debonding is that fiber pullout occurs when a crack initiated at the fiber is unable to propagate into the tough matrix, whereas fiber debonding takes place when a matrix crack is unable to propagate across a fiber [Agapi]. Fiber pullout is usually accompanied by matrix delamination. In fiber debonding, on the other hand, no matrix delamination takes place. Both mechanisms, fiber debonding and fiber pullout, significantly enhance fracture energy, and consequently, the toughness of the composite. Figure 4-6 shows fiber debonding and fiber pullout in a unidirectional carbon-pre-plied composite.

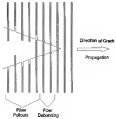


Figure 4-6. Fiber pullout and debonding in a unidirectional continuous fiber composite [Augat].

Fibers break when their fracture strain is reached [Agar00]. When a crack propagates in a direction normal to the fibers, fiber fracture will eventually take place for complete separation of the laminae. Brittle fibers have low energy-absorbing capability because they have a low fracture strain. Although fibers are responsible for enhancing the strength of the composite, fiber fracture accounts for only a small fraction of the total energy absorbed.

In order for the fracture of the composite to be completed, the matrix material surrounding the fiber has to fracture [Agar00]. Brittle matrices can undergo only a limited deformation, while ductile matrices can undergo extensive plastic deformations. Both cracking and plastic deformation absorb energy. However, the energy required for plastic deformation is much higher than that for cracking. Therefore, the contribution of ductile matrices to the total absorbed energy is significant, whereas the contribution of brittle matrices is relatively insignificant.

CHAPTER 3 EXPERIMENTAL PROCEDURE

Alumina Sol Preparation

Trimethyl orthosilicate (TEOS) was used as a precursor for silica, and aluminum-*n*-octanoate (ASO) was the precursor for alumina. Two types of solvents were tested for the silica sol, *n*-heptane and ethanol, while for alumina sol, only *n*-heptane was used as a solvent. It has been observed that there is large difference in the hydrolysis and polymerization rates between TEOS and ASO [104,114]. Hydrolysis and polymerization rates of ASO is much higher than that for TEOS [104,114]. In order to decrease the difference of the hydrolysis and polymerization rates, alumina precursor is not generally hydrolyzed prior to mixing with silica sol while, the silica precursor is partially hydrolyzed. A chelating agent was added to the alumina sol to control hydrolysis and to assist in forming a polymeric sol. Two types of chelating agents were used in the process, triethanolamine (TEA) which is an alkaneamine, and acetylacetone (AcAc) which is a β -ketoester.

Figure 3-1 shows the experimental procedure for the study. Alumina sol preparation was done in a controlled environment (furnace) in which the humidity was maintained at very low levels. The controlled environment was needed to prevent the hydrolysis of ASO by humidity. First, the chelating agent and ASO were diluted separately with *n*-heptane. Chelating agent/ASO molar ratio (R) was varied



Figure 3.2. Flowchart for the experimental procedure.

in different experiments. Second, the chelating agent solution was added drop-wise to the ASN solution which was being stirred vigorously. After adding the chelating agent solution, the solution was stirred for 24 hours to ensure homogeneity.

The silica sol was prepared by diluting TEOS in a solvent. A mixture of DI water and solvent was then added to the solvent. The water to TEOS molar ratio was 2. The hydrolysis step was carried out by heating the sol to 50°C for 40 minutes in a water bath and was allowed to cool. Finally, the silica sol was added drop-wise to the alumina sol inside the dybox while stirring. The sol mixture (silica sol) was stirred for 24 hours to ensure homogeneity. Solution concentrations were selected to yield an 70-75 wt% alumina/20-25 wt% silica composition after heat treatment. Table 5-1 shows the composition of the different sols used.

The silica sol was condensed by heating to 50°C/40°C and simultaneously applying a vacuum. Condensation was unassisted and the sol was filtered through a 1 micron filter. The filtration step was introduced to remove impurities and, in some cases, precipitates. Precipitate and impurity free clear sols were required for successful fiber spinning. The sol was further condensed until the rheological conditions for continuous spinnability were achieved.

Fiber Spinning and Aging

The sol with the right rheological conditions was poured into a container (inside the spinbox). A cup-shaped spinneret with 40 pin holes was used. A

Table 3-1. Sample Identification of Soils Used in this Study with Their Compositions.

Sample ID	Soil Soil Source	Chelating Agent	Si-Value
STC01	soy based	TDA	0.3
STC10	ethanol	TDA	0.3
STC11	ethanol	TDA	1.0
STC12	ethanol	AcAc	0.15
STC13	ethanol	AcAc	0.1
STC14	ethanol	AcAc	0.0

nitrogen pressure of 2 - 4 MPa was then applied on the air inside the nozzle spinneret. The fibers extruded from the spinneret were wound on a rotating drum (driveline) with 15.2 cm diameter. The fiber spinning rate varied between 9.43 m/min. and 42.41 m/min. The spinning rate was controlled by the motor speed. A schematic of the fiber spinning assembly is shown in Figure 1B.

After completing the spinning process, the fibers were removed from the drum and were placed into a 100% humidity chamber for aging. Aging was carried in this study using vapor rather than a liquid. Room temperature and high temperature aging were studied out. The room temperature aging was conducted in a sealed plastic box with water immersion bath. High temperature aging was conducted in a sealed furnace with water immersion bath. Different aging times and temperatures were tested.

Aging and Characterization

After aging was completed, the fibers were placed in a furnace in an alumina substrate and heated to air. The fibers were heated to 600°C (10°C/min heating rate) and held for 2 hours to remove oxygen. Following that, the fibers were heated to 900°C (10°C/min heating rate) and held at that temperature for 30 minutes to complete annealing. The fibers were then heated to 1300°C (10°C/min heating rate) and held for 30 minutes to complete crystallization and densification. Other heating schedules were used in different parts of this study.

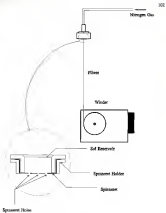


Figure 3-3. Schematic of fiber spinning assembly

Various characterization techniques were used in different steps of the process. These include:

- Fourier transform-infrared spectroscopy (FT-IR),
- viscosity measurement,
- thermogravimetric analysis/differential thermal analysis (TGA/DTA),
- x-ray diffraction (XRD),
- chemical (acid) etching,
- surface density measurement,
- transmission electron microscopy (TEM),
- scanning electron microscopy (SEM), and
- tensile strength measurement.

The FT-IR was used in transmission to detect hydrolysis *in-situ* sol (i.e., if alcohol groups were present). A viscometer was used to measure the viscosity and shear stress change with shear rate for the molten sol. Viscosity measurements were used to determine sol structure and the conditions for maximum operability. Viscosity measurements were also used to determine the effect of different factors (pH value, time, etc.) on sol rheology. Organic removal and surface formulates were investigated using TGA/DTA. Determination of the crystalline phases was carried out using XRD. Glass phase detection was carried out by chemically etching fibers. Chemical etching was carried out by immersing the fibers in 50% HF solution for 10 minutes.

Syndiotactic density measurements on short fibers were used to determine the densification behavior of fibers. Transmission electron microscopy was used to detect the presence of intergranular glass phase. TEM samples were prepared by cutting fibers in an epoxy matrix. The body was cut into thin slices, polished down to 100 microns, then thinned further by dipping and ion milling.

Scanning electron microscopy was used to short fibers to observe the microstructure of fibers prepared under different conditions. The technique was used in combination with chemical etching to determine the presence of a glass phase. It was also used to determine grain growth as a function of time and temperature.

Tensile strength measurements were used to characterize fiber strength after drying. Single fibers were fixed on a rectangular sheet of paper using wood glue, as shown in Figure 5b. The center part of the paper was cut out, and the edges were left to hold the sample. After mounting the sample on the tensile test instrument, the paper edges were cut so that the fiber would carry the complete load during the measurement. A gauge length of 1 cm was used for the fibers.

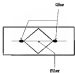


Figure 3-3 Schematic of a tensile strength test specimen.

CHAPTER 6 RESULTS AND DISCUSSION

Chapter Outline

This chapter describes the experimental investigation into process development for producing continuously spinning mullite fibers via the sol-gel process. A discussion of the results of the investigation is presented. The first section deals with the different aspects of the chemical processing of mullite sol components with emphasis on the effect of fiber pre-spinning hydrolysis on fiber properties.

In the second section, the results of the rheology study are presented. This study investigates the following:

- effect of solvent content and residence spinning conditions.
- change of rheological conditions with time
- fiber sol solvent effect on mullite sol rheology
- role of R values.

The third section discusses the TGA/DTA results for various sols. The effect of aging on properties, mullite formation, and fiber microstructure is discussed in the fourth section. This section also discusses high temperature aging.

The fifth section deals with the classification behavior of fibers and the effect of aging temperature on fiber density. In the sixth and seventh sections, crystalline

phase determination and glass phase detection results are presented. The eighth section discusses grain growth in molten fibers as a function of time and temperature. In the ninth section, strength measurement results are presented. In the final section, the results of this study are compared to the results achieved by other investigators.

Chemical Processing of Molten Sol.

The effect of different types of solvents on fiber characteristics and on the fluid properties of molten fiber was investigated. The goal was to determine the effect of pre-spinning hydrolysis of silica sol on the properties of fiber spun. The two solvents tested were *tert*-butanol and ethanol. These two solvents were selected because TEOS has different hydrolysis rates in them. When *tert*-butanol was used as a solvent, no significant hydrolysis was observed. The FT-IR results for silica sol heated at 60°C for 60 min, as shown in Figure 8-1, indicate that hydrolysis did not take place. The associated 3650 cm⁻¹ absorption band which corresponds to the silanol O-H stretching vibration (indicative of hydrolysis) was not observed. Similar results were observed when the silica sol was heated at 60°C for 3 and 4 hr.

The absence of silanol groups had an adverse effect on the formation of the polymeric structure (which is required for fiber spinning)-no polymerization after mixing with the alumina sol. The molten sol made from the silica sol was labeled "TEOS". Fibers drawn from this molten sol had a very poor gross strength. The term "poor gross strength" was used to categorize fibers that broke into small pieces prior to being spun. The term "good gross strength" was used to categorize fibers which

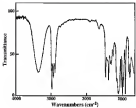


Figure 4-1 FT-IR spectrum for silica sol with non-formal solvent heated at 65°C for 60 minutes

maintained integrity before being. The fibers in which hydrolysis and polycondensation reactions were incomplete were characterized by weak, brittle fibers post firing at 1200°C. Poor green strength was a result of the absence of polymer chains. The poor quality of fired fibers was a result of a poorly networked and homogenized green structure.

Figure 4-3 is a SEM micrograph of a fiber made from the STBL2 sol with a short hydrolysis time of 4 hours. As shown in the micrograph, a large whisker-shaped grain and large pores were present. The poor mechanical properties observed for these fibers can be attributed to the microstructure of the fiber, which resulted from the absence of molecular-scale bonding due to the poor hydrolysis of TBOS.

When ethanol (which is normally used as preparing solvents) only was used as a solvent, a pronounced hydrolysis was observed. Results obtained by FTIR for the silica sol heated at 60°C for 60 min showed the presence of the 3675 cm^{-1} absorption band, as shown in Figure 4-4. The formation of silanol groups, as a result of hydrolysis, is essential to the formation of the polymeric structure produced when reacting with ethanol sol. A minimum water/TBOS molar ratio of 2 was required to form the desired polymeric structure. A 3-dimensional network structure is produced at higher water/TBOS molar ratios [Saito]. Molar sols made from this silica sol were labeled 'ETBL2'. Fibers extruded from this molar sol had good green strength, were flexible, and strong after being at temperatures above 1200°C.



Figure 6-2. SEM micrograph of a fiber made from STO3 and 10 wt% polyacrylate, dried at 140°C.

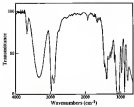


Figure 4.3 FT-IR spectrum for silane with enhanced solvation heated at 60°C for 10 minutes.

The good grain strength can be explained by considering hydrolysis and polymerization reactions. The bifunctionality of the partially hydrolyzed TUDS group (which is a result of using water/TUDS ratio of 2) and the high polymerization rate of aluminum alkoxide promote the formation of polymer chains by the polymerization of partially hydrolyzed alumina species and the unhydrolyzed aluminum species. The good characteristics of the dried fibers were due to the homogeneity obtained from having extensive hydrolysis and polymerization reactions. Figure 8-4 shows a SEM micrograph of a needle fiber made from the ETULi sol. The grains were mostly equiaxed and no whisker shape grains were observed.

The difference in the TUDS behavior for the two different solvents can be explained by considering the hydrochloricity and the hydrolytic assistance of the different alkoxy groups. When acetone is used as a solvent the following reaction takes place



The nucleophilicity of the $(OC_2H_5)_2$ is greater than that of $(OC_3H_7)_2$ [16-18]. Therefore the concentration of $(OC_2H_5)_2$ hydroxyl increases progressively after mixing. Since the resistance to hydrolysis increases with an increase in length of the alkoxy group [16-18], a slower hydrolysis is expected when the metal ligand is $(OC_2H_5)_2$ rather than $(OC_3H_7)_2$. When ethanol is used as a solvent, the metal ligand $(OC_2H_5)_2$ does not change, since the interaction of the ligand with the solvent yields the same product as the reaction. Consequently, hydrolysis is faster



Figure 4-4. SEM micrograph of a surface layer from ST113 apf with 0.1M NaBiotolyne, 1 hour, fixed at 100°C.

where ($\delta\text{C}_2\text{H}_2$) is the signal signal due to the ethylene chain length of the polymer ($\text{P}_{\text{C}_2\text{H}_2}$).

To investigate the possibility of performing hydrolysis after spinning, a solution was prepared without water. The chloro sol was mixed with an aluminum sol and condensed to the proper viscosity for spinning. The fibers spun from the mixed sol were difficult to handle due to very low gear strength. This may show that the evolution of an interconnected polymeric structure prior to spinning is necessary to produce good quality fibers.

For all the methods used to prepare the master sol, a precipitate free and transparent sol was a prime consideration. The presence of precipitate has a detrimental effect on the consistency of the fiber spinning process since the precipitate becomes and clog the spinneret holes, impeding the spinning process. Precipitates were formed when water was introduced along with triethanolamine (TEA) to the aluminum-oxo-bisacetoxy (AOB) solution, and when water was added to the master sol.

It is believed that the formation of precipitate is attributed to the right hydrolysis and precipitation of AOB.



Rheology Study

Effect of Solvent Content and Crosslinked Spacing Conditions

The rheological behavior of the emulsion gel as a function of solvent content was investigated. In addition, the rheological conditions for coagulation spacing were determined. A variety of viscosity ranges were realized by evaporating solvent during the coagulation step. Figure 6-6 shows plots of shear stress versus shear rate and viscosity versus shear rate for the emulsion gel (EDDS) which had retained no free sol solvent and THF as the diluting agent with a dilution agent/EDDS molar ratio (P) of 5.3. The three plots shown in Figure 6-5 correspond to three EDDS gels with different amounts of solvent removed. The gel with high volume content of solvent exhibited Newtonian behavior (plot 1), in which the viscosity was shear rate independent. This behavior was due to the insignificant interaction between gel clusters.

When the solvent amount was decreased by condensation, the gel exhibited a shear thinning behavior (plot 2), in which the viscosity decreases with increasing shear rate [Sedif]. The decrease in the viscosity with the increase of shear rate can be attributed to the release of the associated solvent within clusters after they break [Sedif]. Further condensation resulted in a gel with thixotropic behavior (plot 3). Thixotropic behavior occurs when a three-dimensional network is formed that with thixotropic behavior has an elastic character. After the yield stress is exceeded,

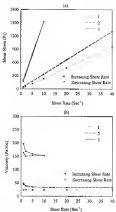


Figure 4-3. Plots of a) shear stress versus shear rate, b) viscosity versus shear rate for ETLJ gel. Plot 1 corresponds to high solvent content, Plot 2 corresponds to medium solvent content and Plot 3 corresponds to low solvent content.

shear thinning behavior is accompanied by hysteresis [Bard77]. This behavior indicates that the broken network was not recovered when the shear rate was decreased.

It was observed that in order to achieve continuous spinning, slightly shear thinning behavior is required. The soil corresponding to plot (b) exhibited maximum spinability. Also, the fibers spun from this soil had very good gross strength. Soil with rheotropic behavior exhibited poor spinability but reasonable gross strength. On the other hand, soil with Hookean behavior exhibited reasonable spinability but broke down easily prior to spinning. This poor gross strength is due to the absence of a continuous structure. These results are also consistent with previous observation for other soil [Bard77].

Change of Rheological Condition with Time

The change of rheological behavior of sodium soil spinel at 4°C with aging time was studied. Figure 6-6 shows plots of shear stress versus shear rate and recovery versus shear rate for E70.1 soil immediately after undraining and 1 day after undraining. It was observed that the viscosity increased with time. However, the shear thinning behavior was maintained. Soil made with acrylamide (AcA) as a stabilizing agent with $R=0.11$ (labeled "E70.1P") exhibited a different behavior. Figure 6-7 shows that E70.1P soil did not show a significant change in viscosity even after 30 days. However, a change was observed in the viscosity behavior and the soil became highly rheotropic after 30 days. The change in behavior may be attributed to the low R value used in the mixture. Small R values generally result in a smaller

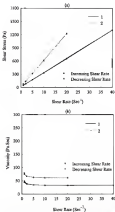


Figure 4-6. Plot of (a) shear stress versus shear rate, (b) recovery ratio shear rate for SBR3 gel. Plot 1 measurement taken immediately after shearing. Plot 2 measurement taken 5 days after shearing.

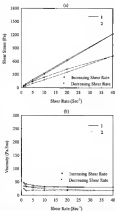


Figure 6-7. Plots of a) shear stress versus shear rate, b) viscosity versus shear rate for EAFB15 soil. Plot 1 measurement taken immediately after compaction, Plot 2 measurement taken 18 days after compaction.

fraction of hydrolysis sites being blocked. As a result, hydrolysis and polymerization can coexist and lead to a three-dimensional network with rheological behavior.

Effect of Solvent on Melt Rheology

The effect of other solvents on molten oil rheology was investigated. Figure 6-6 shows the rheological behavior of molten oil with two different other oil solvents, *tert*-butanol and ethanol. The molten oil study with *tert*-butanol as other oil solvent and TGA as stabilizing agent with R=0.2 was labeled "TBOL". This oil showed a Newtonian behavior, while ETOA, which used ethanol instead of *tert*-butanol as the other oil solvent, exhibited shear thinning behavior. These results can be explained by considering the effect of other oil solvent on the hydrolysis of TGA that was presented in the preceding section. When *tert*-butanol was used, no significant hydrolysis was observed. As a result, structure evolution was very limited, and cluster interaction was minimal, which resulted in Newtonian behavior. On the other hand, when ethanol was used, hydrolysis was observed, and cluster growth took place as a result. The breaking of these structures and the release of the entrapped hydroxyl resulted in the shear thinning behavior.

The Role of R Value

The effect of the molar ratio R on the oil rheological behavior was studied using *tert*-butanol and ethanolamine as stabilizing agents. When ATOA was used

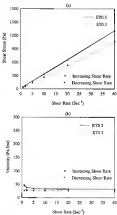


Figure 6-8. Plots of a) shear stress versus shear rate, b) viscosity versus shear rate for ET92.3 and ST92.3 soils.

as the thickening agent, low values of R (<0.3) resulted in thixotropic soils which settled readily when exposed to air. On the other hand, high values of R (>0.5) resulted in approximately Newtonian behavior. In addition, precipitation formation was observed in these soils. The optimum R value for maximum spontaneity and good stability of the soil was approximately 0.3. Figure 6-4 shows that the soil with $R=0.3$ (ETR0.3) exhibits a slightly shear thinning behavior. The figure also shows that soils with $R=0.15$ (ETR0.15) exhibit thixotropic behavior, and soils with $R=0.6$ (ETR0.6) display Newtonian behavior. The thixotropic behavior was a result of the small fraction of hydrolyzed sites blocked by the thickening agent, and the Newtonian behavior was a result of the large fraction of blocked hydrolyzed sites.

When TGA was used as the thickening agent, similar results were observed. Figure 6-10 shows that for soil ET1, which had a $R=1$, Newtonian behavior was observed. No precipitation formation was observed in this soil. Soils with $R=0.3$ (ETR0.3) exhibited a slightly shear thinning behavior, and possessed a very good spontaneity.

The effect R value has on the behavior of soils with different solvent contents was investigated. Figure 6-11a shows that E700.3 soil exhibited a change in behavior from Newtonian to shear thinning upon condensation of the soil. Soils with $R=1$ (ET1) on the other hand, did not show any change in the rheological behavior (from Newtonian behavior) upon condensation (Figure 6-11b). This result can be explained by considering the role played by the thickening agent. As mentioned previously, the thickening agent acts as a barrier toward the hydrolysis process by blocking hydrolysis

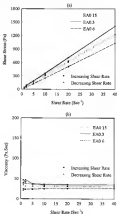


Figure 4-8. Plot of a) shear stress versus shear rate, b) viscosity versus shear rate for BAG 15, BAG 23, and BAG 8 gels.

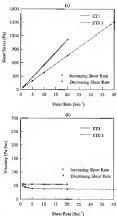


Figure 4-10: Plots of a) shear stress versus shear rate, b) viscosity versus shear rate for ETI-3 and ETI soils.

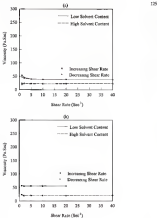


Figure 6-11. Plots for viscosity versus shear rate for (a) EDD1 oil and (b) EDD1 oil

the solvent content was decreased and cluster growth took place. When $\bar{N}=1$, the \bar{M}_w was 1. As \bar{N} increases, the fraction of available hydrolysis sites decreases. The smaller the fraction of available hydrolysis sites, the more limited the growth of clusters. For the case with a $\bar{N}=0.2$, the fraction of blocked hydrolysis sites was small. As a result, cluster growth was not restricted. Shear thinning behavior resulted when fraction of blocked hydrolysis sites was large. Consequently, cluster growth was restricted and the behavior remained Newtonian when the liquid content was decreased.

Thermal Analysis Study

Thermal analysis study was carried out using simultaneous TGA (thermogravimetric analysis) and DTA (differential thermal analysis) analyses. Results of TGA/DTA analysis were used to determine the temperature range over which weight loss of fibers took place due to removal of organic and dehydroxylation. In addition, DSC results were used to determine melting transformation temperature. Figures 6-11 show TGA/DTA results for fibers from ECP-3 unaged for 36 hours at room temperature. As shown in the figure, the weight loss occurs at approximately 450°C. Melting transformation is observed at about 600°C, which is shown as the sharp exothermic peak. The melting transformation temperature is typical for single phase melting gel.

While clustering repeats play a beneficial role in developing the desired rheological characteristics for fiber spinning, they induce other effects during

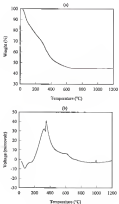


Figure 4-12: a) TGA and b) DTA results for E794.3 fibers aged for 24 hours at room temperature.

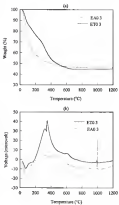


Figure 4-11. (a) TGA and (b) DTA results for E403 and E703 fibers aged for 30 hours at 100°C.

subsequent porosity. Therefore, the effect of dehalting agent on weight loss and mullite formation was investigated using TGA/DTA analysis. Figure 6-10a shows removal of organics was completed at lower temperatures with AAKa than with TGA. At 200°C, the ETG1.0 fibers had lost approximately 75% of the initial weight loss, while the ETG1.0 fibers had lost only 40% of the total weight loss. Removal of organics and hydroxyl groups at low temperatures is important because it reduces the possibility of foaming and residual porosity due to gas evaporation. Foaming, or blooming, can occur if spinning takes place before the complete removal of volatile. Figure 6-10 shows blooming and the presence of porosity in ETG1.0 sol fibers that was heated quickly to 1200°C without allowing organics to be removed.

The effect of the dehalting agent on mullite transformation was also investigated. As shown in Figure 6-10b, both samples, ETG1.0 and ETG1.0, have mullite transformation peaks at approximately 1000°C. However, the peak intensity is about 8 times larger in the case of AAKa (sample ETG1.0). These results indicate a significant enhancement in mullite formation when the AAKa is used. The enhancement in mullite formation may be attributed to more uniform mixing (on a molecular scale) achieved in sol prepared with AAKa.

Conclusion

Prior to fiber spinning, the sol is only partially hydrolyzed. Consequently, an aging step following spinning is of significant importance. The aging step aids in completing hydrolysis and polycondensation of the gel, and it can have an influence



Figure 6.14. SEM micrograph for EDR3 fiber aged for 20 hours at room temperature and fixed at 1500°C with heating rate of 15°C/min.

on the properties of the fiber fiber. It was observed in this study that fibers that were not aged were fully brittle, and very weak. These fibers retained a black color, indicating of the presence of tensile carbon at temperatures as high as 1100°C.

Figure 6-15 shows the microstructure of a E462 soil fiber that was not aged. The presence of a significant porosity and irregular large grain is evident. The porosity can be attributed to the removal of volatiles at high temperatures rather than low temperatures (below melting temperature). This can cause incomplete sintering. Figure 6-16 shows weight loss measured above 1000°C for the unaged fibers. The presence of large irregular grain among small equiaxed grains may be attributed to the absence of molecular-scale homogeneity in the gel prior to crystallization. Aging can help in lowering the temperature of volatile removal. Figure 6-17 shows that while volatile removal for unaged fiber continued to above 1000°C, weight loss was ceased at about 600°C for aged fibers. Figure 6-17 shows the microstructure of E462 soil fiber aged at 100°C. The microstructure of the aged fiber does not show the presence of porosity. Also, a majority of the grains were small and equiaxed. No exaggerated grain growth, similar to that in the unaged fiber, was observed.

The role of aging time on volatile formation was investigated. Figure 6-18 shows DSC results for E462 soil fibers with different aging treatments. For unaged fibers, the 100°C peak was not detectable. Fibers aged for 3 hours exhibited a small endothermic peak at temperatures slightly above 100°C, and a larger peak was detected for fibers aged for 24 hours. Both samples were aged in room temperature.



Figure 6-11: SEM micrographs for unaged D403 fiber (heat at 1500°C for 30min).

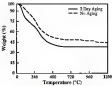


Figure 6.16. TGA results for aged and unaged EPO films.



Figure 6-17 SEM micrograph of an SAE10 steel aged at 100°C with no hold time and observed at 1500°C for 10 min.

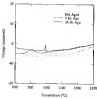


Figure 4-10. DTA results for ETRJ fibers with different aging times.

These results indicate that longer aging time enhance molite formation. These results can also be explained in terms of fiber homogeneity. Absence of micro-scale heterogeneity resulted in an undesirable molite transformation for the unaged fibers because of the lack of local reactivity at the reaction temperature. The enhancement in the molite formation with increasing aging time can be attributed to the improvement in the micro-scale heterogeneity. This improvement in homogeneity is a direct result of hydrolysis and polycondensation reactions taking place during aging.

The role of aging temperature on fiber microstructure was studied. It was observed that aging temperature had an important effect on fiber grain size. High aging temperatures produced smaller grain sizes. Figure 6-19 shows the microstructure of room temperature aged ETBL3 and fibers (24 hr aging time), and the microstructure of the same fibers aged at 100°C (with no hold time). A significant difference in the grain size was observed. Similar microstructure was observed for ETBL3 and fibers aged at 100°C (Figure 6-20). Fibers from ETBL3 and aged at 80°C showed a significantly larger grain size (Figure 6-21).

Upon examination of both types of fibers aged at 100°C, the ETBL3 fibers (that were made with ABA as the chelating agent) were found to be strong and durable, while ETBL3 and fibers (that were made with TGA as the chelating agent) were weak and brittle. Density of the ETBL3 fibers was 2.7 g/cm³ while the density of ETBL2 fibers was 3.1 g/cm³. Examination of ETBL3 fiber ends showed a significant separation between an outside inelastic shell and an inside fiber core.



Figure 8-18. SEM micrographs of EPOD fibers a) aged at room temperature for the fibers b) aged at 150°C with no hold time. Both fibers were sintered at 1500°C for 10 min.

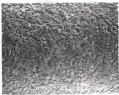


Figure 6-20. SEM micrograph of an EVA/3 fiber aged at 100 °C with no hold time and annealed at 150 °C for 16 min.

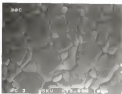


Figure 4-25: SEM micrograph of an SLM 316L steel aged at 400°C with no hold time and annealed at 1300°C for 1h.

(Figure 6-22). The structure resulted in the poor mechanical properties of these fibers. Figure 6-23 shows a uniform microstructure across the fiber and the absence of large pores in EA63 fibers.

These results can be attributed to the difference in the aging (hydrolysis and polycondensation) rate between the two fibers. Fibers made with AcAc as a stabilizing agent complete aging faster than fibers made with TGA. The variation in the extent of aging across the fiber in the case of EA73 fibers resulted in a dense outside shell and a porous inside core. In contrast, EA63 fibers did not show a difference in the microstructure across the fiber, since no significant variation in aging existed. These results indicate that AcAc is a better choice of stabilizing agent at high temperature aging, to be used.

Maintaining a constant aging temperature, the effect of R value on grain size was investigated. Fibers from mix EA63 and EA64 (corresponding to R=0.5 and R=0.6 respectively) were aged at 20°C and fixed at 1000°C. A comparison between Figures 6-23 and 6-24 show that EA63 fibers had a significantly larger grain size than EA64 fibers. The small grain size of the EA64 fibers was a result of the chlorine agent's effect on hydrolysis. High R values resulted in smaller fractions of hydrolysis sites, and consequently, a smaller fraction of polycondensation sites. The small fraction of polycondensation sites decreased cluster growth in the sol. As a result, small grains were produced upon firing.

High temperature aging has the following advantages when used in production of EA63 fibers:

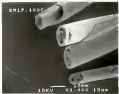


Figure 6.22 SEM micrograph of ETBL2 fibers aged at 100°C with no hold time and measured at 100°C for 10 min.

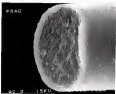


Figure 6-23 SEM micrograph of an E400.2 fiber aged at 200°C with no hold time measured at 1500°C for 10 min.



Figure 6-24 SEM micrograph of an SAE 1003 steel in 89°C with no hold time and annealed at 1300°C for 10 min.

- increases reaction kinetics, and as a result, aging time can be reduced. This point is crucial when considering a continuous spinning process.
- improves intra-fiber homogeneity, and as a result, fibers are produced with relatively small grain size. Small grain size fibers are desirable when achieving high strength is required.

Deactivation Study

Apparent density measurements were carried out for the EA63 and ET63 fibers aged at room temperature for 24 hours and fired at different temperatures with a heating rate of 10°C/min. Figure 6-25 shows the difference between the two types of carbon fibers. The error bars were not shown in the figure due to the very small value of the standard deviation ($n = 100,177$). At temperatures below 1000°C, EA63 fibers had lower density than ET63. This may be a result of the removal of oxygen at a lower temperature as was the case for EA63 fibers, as discussed earlier.

Significant increase in the density occurred in both samples above 1000°C due to viscous flow sintering. The sintering rate was faster for the EA63 fibers. At a temperature of 1600°C, EA63 reached about 90% of its final density, while the ET63 fiber reached approximately 80% of final density. Figures 6-26 and 6-27 show polarized sections of EA63 and ET63 fibers fired at 1500°C. Some porosity was observed in the ET63 fiber, but none was observed in the EA63 fibers. Figure 6-28 shows an unpolarized section of ET63 fiber with large pores present.

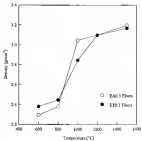


Figure 4-25: Densification curves for E613 and E703 fibers aged for 24 hours at room temperature.

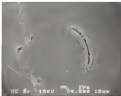


Figure 6-2b. SEM micrograph for a polished-cross section of 500 nm thick fiber annealed at 200°C for 30 min.



Figure 4-27. SEM micrograph for a polished cross section of E783 fiber heated at 1300°C for 10 min.



Figure 6-10 SEM micrograph of an E7013 fiber measured at 1000°C for 10 min.

It was observed that the final apparent density depends on aging temperature. Fibers aged at 400°C and 1000°C had apparent densities of 3.9 and 3.3 g/cm³, respectively after sintering at 1500°C for 30 min. This change in density with aging temperature is attributed to the extent of aging reached at a certain temperature. The higher the aging temperature, the higher the vapor pressure. Also, aging reaction kinetics are enhanced at high temperatures. Therefore, high aging temperatures produce fibers with low organic content, and consequently, low-organic material was removed during fiber pressing; higher densities.

Cryocrystal Phase Determination

Cryocrystal phase determination was carried out using x-ray diffraction (XRD). The XRD pattern for pure cellulose powder shown in Figure 4-29 was used as a reference to determine if cellulose was the only phase formed in the fiber. Fibers from E4M3 and ETI13 soils were fixed at 1000°C, which is slightly above the maximum observed in the DTA curve. Both samples showed patterns (Figure 4-29 and 4-30) identical to the pure cellulose pattern shown in Figure 4-29. Fibers from the same soils were fixed at 1500°C and showed patterns identical to the ones in Figures 4-29 and 4-31. These results show that there was no phase transformation above 1000°C from another crystalline phase to cellulose. The results indicate that the 860°C maximum corresponds to cellulose formation, and that cellulose was the only crystalline phase present. The patterns of XRD peaks and their intensities for ETI13 fibers fixed at 1500°C, for pure cellulose powder, and for the standard AFM10 peaks are presented in Tables 4-1, 4-2, and 4-3. The results shown in Tables 4-1 and 4-2 indicate that

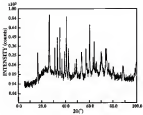


Figure 4-30 XRD pattern for pure malonate powder

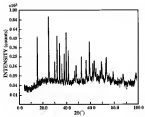


Figure 8-10. XRD pattern for 0.433 glass fired at 1000°C.

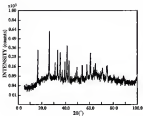


Figure 6-31. XRD pattern for E703 glass heat treated at 1000°C.

Table 4-1. Positions of XRD peaks and their intensities for STO3 film.

Peak Number	Angle (2θ) (°)	Intensity (%)
1	8.345	2.28
2	16.448	24.94
3	26.005	67.58
4	26.305	52.98
5	30.025	21.67
6	30.255	24.98
7	35.300	14.56
8	37.083	17.08
9	38.320	30.32
10	48.900	100.00
11	52.475	37.87
12	49.140	19.23
13	49.463	17.73
14	53.483	12.41
15	53.985	22.66
16	57.625	34.22
17	58.375	19.97

Table 4-2: Positions of XRD peaks and their intensities for pure mullite powder

Peak Number	Angle (Degree)	Intensity (%)
1	30.459	30.96
2	26.875	31.09
3	26.350	31.35
4	31.072	29.54
5	33.305	32.64
6	35.348	21.42
7	31.085	21.05
8	34.328	20.99
9	40.953	16.00
10	41.620	14.64
11	43.279	13.76
12	49.553	17.72
13	53.548	17.16
14	53.979	20.92
15	57.942	25.23
16	58.413	13.00

Table 4-3 Positions of XRD peaks and their intensities for the standard ASTM peaks.

Peak Number	Angle (Degree)	Intensity (%)
1	10.402	99
2	23.594	8
3	25.971	95
4	26.267	100
5	32.960	39
6	33.224	49
7	35.278	59
8	36.903	14
9	38.993	4
10	39.296	39
11	40.874	60
12	42.590	79
13	42.868	8
14	43.899	2
15	47.227	2
16	48.554	8
17	49.468	19
18	50.462	6
19	50.863	19
20	54.059	19
21	57.564	29
22	59.412	12

multi-fiber peaks match all multi-polymer peaks with very small difference in peak position (maximum difference in peak position = 0.05°). Comparing Table 4-3 to Table 4-1, all peaks with intensity > 1% in the ASTM file matched the multi-fiber peaks with very small difference in peak position (maximum difference in peak position = 0.05°).

Glass Phase Detection

The presence of an amorphous glass phase in multi-fiber can result in detrimental effects on high temperature properties of the fibers. The amorphous glass phase causes a deterioration in the creep resistance of the fibers, this limits their use at high temperatures. Since the main application for multi-fiber is at high temperatures, production of glass-free multi-fiber is crucial.

Two techniques were used for glass phase examination, chemical etching and transmission electron microscopy (TEM). The chemical etching technique is based on the large difference in the dissolution rate of the amorphous glass phase and cellulose in hydrofluoric acid (HF). The glass phase dissolves readily in HF while cellulose has a very low dissolution rate [See??]. The chemical etching experiments were carried out by immersing fibers in 10% HF solution for 10 minutes. Micrographs were taken using SEM before and after the etching treatment to determine if there were differences at the macroscopic level. Fibers produced by the processes developed in this study were compared to commercially available multi-fiber fibers.

Figures 4-3(a,b) and 4-3(a,b) show ETB-3 and Nason 400 fibers before etching at different magnifications. Figures 4-3(a,b) and 4-3(a,b) show the fibers after the

(a)



(b)



Figure 6-12. SEM micrographs of an E703 fiber before stretching (a) at 2000X and (b) at 1500X.

(a)



(b)



Figure 4-11. SEM micrographs for a Novel 400 fibers before cycling a) at 2000K and b) at 1900K.

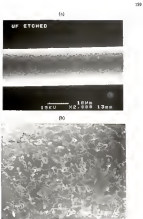


Figure 4.14. SEM micrograph for an etched STO3 fiber a) at 2000X and b) at 5000X.

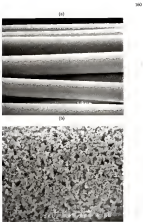


Figure 4-25. SEM micrograph for stacked Kevlar 445 fibers a) at 20000x and b) 50000x.

etching treatment. No discernible difference was observed in the microstructure of ET703 fiber after etching, indicating that there was no significant amount of glass phase present. In contrast, Novol 400 fibers exhibited a significant difference in the microstructure after etching. The etched Novol 400 fibers showed a network of porosity that reached from the dissolution of the glass phase. These results indicate that Novol 400 fibers contain a large amount of glass phase. Figure 6-16 shows the microstructure of an etched Alax fiber produced by Sorenson company. Alax fibers contain 33 wt% silicon and 67 wt% aluminum. Although the Sorenson fiber composition has a lower silicon content than the fibers produced in the study, the etching treatment resulted in the dissolution of an amorphous glass phase, as shown in Figure 6-16. Results for ET403 fibers were similar to those obtained for ET703 fibers. Figure 6-17 indicates that there was no discernible amount of glass phase present in these fibers.

Micrographs taken by TEM confirmed the results achieved by chemical etching for ET703 fibers. Figures 6-18 and 6-19 show that no glass phase was present at the grain boundaries or at the triple junction points. Fibers made with an etchanol as the etching solvent (ET703-1a) which, as mentioned previously, had a poor homogeneity, showed the presence of an amorphous glass phase (Figure 6-19). It was observed in this study that the absence of molecular scale heterogeneity of the gel may lead to the presence of an amorphous glass phase.

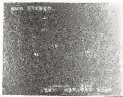


Figure 6(b): SEM micrograph of an etched Al₂O₃ film at 100000x.



Figure 6-31. SEM micrograph of an etched RA63 fiber on Ti6Al4V.



Figure 6.2b. TEM micrograph of an EK0.1 fiber at 200,000 \times . Samples were prepared and micrographs were taken by A. Macrini.

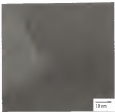


Figure 4-38. TEM micrograph of an E703 fiber at 100,000x. Samples were prepared and micrographs were taken by A. Mermel.



Figure 6-46. TEM micrograph of 5Titch fibers at 100,000X. Samples were prepared and micrographs were taken by A. Mazzoni.

Grain Growth Study

Grain growth can result in detrimental effects on fiber strength if large grains are produced. The strength of polycrystalline materials is inversely proportional to the grain size (Kam)%¹. Since mullite fibers are primarily used at high temperatures, grain growth is expected due to the strong dependency of grain growth on temperature. The grain growth follows the Arrhenius equation (Kam)%¹

$$\frac{dG}{G} = \frac{Q}{RT} \ln \left(\frac{G}{G_0} \right) \quad (4.4)$$

where G = growth rate, G_0 = constant, Q = activation energy for grain growth, R = Boltzmann constant, T = temperature.

The change in the grain size as a function of temperature and time was examined. The grain size was measured using SEM. To measure the grain growth as a function of temperature, EAM2 fibers (pre-sintered at 1300°C) were annealed at different temperatures, but with constant annealing time (1 hour). The results are presented in Figures 4-41. The figure shows that up to 1100°C, there was no measurable increase in grain size for 1 hour hold period. However, a significant increase in the grain size was observed at 1200°C.

The grain growth as a function of time was investigated using EAM2 fibers (pre-sintered at 1300°C). The fibers were annealed at 1200°C for different periods of time. Figures 4-42 and 4-43 show the change in the grain size with annealing time at 1300°C and 1400°C. No significant change in the grain size was observed even

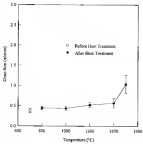


Figure 4-41. Gross RSC versus annealing temperature for PA66 fibers (pre-treated at 200°C) with 1 hour annealing time.

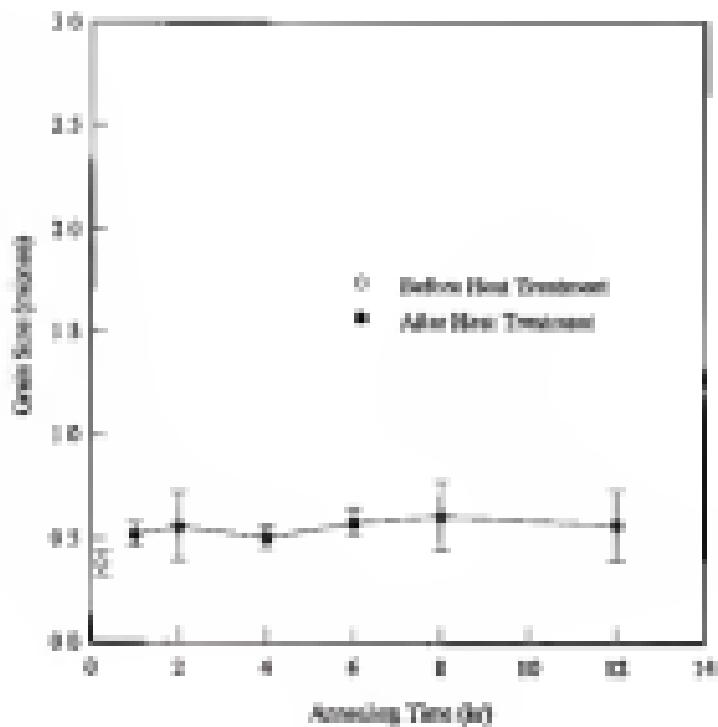


Figure 4-11. Chain flex versus annealing time for X460 fibers (pyrolyzed at 1200°C) with annealing temperature of 1200°C.

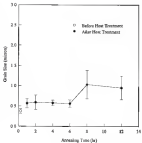


Figure 6-40: Green size versus annealing time for 0.5M3 glass (pre-sintered at 1400°C) with annealing temperature of 1400°C.

for annealing times as long as 12 hours at 1300°C. However, for annealing temperatures of 1400°C, grain growth was observed after annealing times of 8 hours. These results show that the process for grain growth has a high activation energy so that time-dependent growth is not observed at temperatures up to 1300°C. A significant change occurs in 1 hour at 1300°C or in 8 hours at 1400°C.

Strength Measurements

The tensile strength of ETG3 and EAG3 fibers was measured. Both types of fibers were tested at 1300°C. However, ETG3 fibers were aged for 34 hours at room temperature, while EAG3 fibers were aged at 1300°C with no hold time. Many of the ETG3 and EAG3 fibers failed near the area where the glue was applied. No strength values were reported for these fibers as the results were not representative of the tensile strength of the fibers. Results are reported only for fibers that failed at regions other than the glue interface.

The tensile strength of fibers was calculated by the equation:

$$\sigma_t = \frac{F}{r^2 d^2} \quad 6.3$$

where σ_t = tensile strength, F = applied tension force in ounces, and r = fiber radius. Fiber diameters were 19-21 microns for ETG3 fibers and 17-20 microns for EAG3 fibers.

The measured tensile strengths for the two types of fiber were as follows:

- For ETU fiber: $\sigma_y = 0.26$ GPa

number of samples = 27

number of samples that broke at the middle
during testing = 5

standard deviation = 0.01

- For EAD fiber: $\sigma_y = 0.44$ GPa

number of samples = 26

number of samples that broke at the middle
during testing = 3

standard deviation = 0.01

Only the samples that broke in the middle were taken into account in measuring the fiber strength and the standard deviation. The difference in the tensile strength can be attributed to the difference in grain size and porosity. The average grain size of ETU fiber was about 1.25 microns, while the average grain size for EAD fiber was 0.07 microns. Also, it was shown in a previous section that ETU fiber exhibited some porosity due to the high temperature required for sintering sputtered. The EAD fiber did not exhibit porosity. Preliminary measurements on EAD fiber sintered at 1200°C yielded tensile strength data as high as 1.15 GPa. This is presumed to result from an even smaller grain size.

Comparison Study:

In this section, the results achieved in this study are compared to the results reported previously in the area of sol-gel processing of mullite as well as processing of mullite fibers. It was shown in this study that there was a single phase transformation that occurred at 980°C to form mullite. Some previous studies showed more than one phase transformation before forming mullite.

- Prachanta and King results showed a phase transformation at 980°C to form $\gamma\text{-Al}_2\text{O}_5$ or spinel, and another phase transformation at 1200°C to form mullite [Prachanta and King 1997]
- Park and co-workers results showed a phase transformation at 1000°C to spinel followed by transformation to mullite at 1200°C [Park et al. 1997]
- Ritterich and co-workers results indicated a phase transformation at 1100°C to spinel followed by transformation to mullite at 1250°C [Ritterich et al. 1997]

One of the main objectives of this study was to produce single phase mullite fibers with no intergranular glass phase. Results indicate this objective was achieved. However, other studies reported the presence of more than one phase:

- Park and Kim showed the presence of a glass phase [Park and Kim 1997]
- Holling and Mising showed the presence of tetragonal mullite and glass phases [Holling and Mising 1997]
- Wei and Hulbert showed that mullite produced contained alumina particles [Wei and Hulbert 1997]

- Schaefer and co-workers indicated the formation of γ -Mg₂Si, mullite and mullite in the system they studied [Sch02].
- Scopparis showed the presence of spinel and glass phase [Sco04].
- Fibers of commercial Mullite fibers measured in this study showed an appreciable glass phase.

Production of fibers with equiaxed grains was achieved in this study. Previous studies carried out by Biria and Langford and Li and Thomson produced acicular grains [Bir04, Lin04, and Kra03]. The grain size of fibers produced in this study (0.403 fibers) was 0.31 microns, compared to the 2-4 micron grain size produced by Tolksa and Pandur [Tol02].

Verkouteren and co-workers were able to produce single phase mullite fibers with small equiaxed grains. However, these fibers were short because continuous sinterability could not be achieved [Ver08]. In this study, continuous spinning of fibers was achieved. Taylor and co-workers were able to produce mullite fibers. However, fiber diameter was large (118 microns), the fibers were brittle, exhibited porosity and microcracks [Tau03]. Fibers produced in this study (0.403/f) had small diameter (10-20 microns). These fibers were flexible and did not have porosity or microcracks. Mullite fibers produced by Kim and co-workers had needle-like grain compared to equiaxed grains observed in the study [Kim03]. No reference for grain size, fiber diameter, or fiber strength was found in Baek's work. Also, the presence of an intergranular glass phase was not investigated.

CHAPTER 7 SUMMARY, CONCLUSIONS AND FUTURE WORK

A process was developed to produce continuous multi fibers. The conditions to achieve continuous spinnability and the factors that affect the rheological behavior of molten sol were determined. The optimum value for obtaining spontaneous/generator molten ratio was determined. Also, the effects of changing the rheology agent on organic content, molten formation, fiber aging, fiber classification, and fiber microstructure were investigated. The role of aging in molten transformation and its effect on the properties and microstructure of fibers were determined. In addition, the effect of aging temperature on properties and microstructure was observed. The fibers were tested to determine if there was an interpolymer glass phase and were compared to commercial cellulose fibers. The grain growth was determined as a function of time and temperature.

Conclusions

The following conclusions were drawn from the work done during the study:

- The conditions for continuous spinnability of molten sol were determined. Continuous spinnability was achieved when the sol flow behavior was slightly shear thinning;
- Sol viscosity increased significantly with time but flow behavior remained

the same for soils with moderate values of R ($R = 0.1$). For low values of R ($R = 0.0$), viscosity did not change significantly, but flow behavior was altered:

- Shear thinning behavior was observed when shear hydrolysis occurred, and Bingham behavior was observed when shear hydrolysis did not occur.
- Soils with low R values exhibited thixotropic behavior, while those with intermediate and high R values exhibited shear thinning and Bingham behavior, respectively.

• Change of solvent system resulted in a change in flow behavior for soils with moderate R values ($R = 0.1$), but it did not result in a change in behavior for soils with high R values ($R = 0$).

• Pre-aging hydrolysis of clays did not contribute to achieve good strength for green filters and good microstructure for treated filters. Also, pre-aging hydrolysis of clays did not result in avoiding the formation of an intergranular glass phase.

• Lower temperature of organic removal and significantly enhanced organic transformation were achieved when AKA was used as a claying agent.

• Filter aging was shown to be crucial in attaining quality filters. Unaged filters showed significant porosity and large irregular grains, while aged filters did not show the presence of porosity and the grains were aggregated and small.

- Aging resulted in enhancing particle formation.
- The grain size increased with increasing aging temperature.
- Filter density increased with increasing aging temperature.

- Fibers made with Azoic aged more efficiently at high temperature than those made with TGA.
- The densification rate was higher for fibers made with Azoic than those made with TGA.
- Mullite was the only crystalline phase present above 1000°C.
- Neither fibers made with TGA nor fibers made with Azoic showed the presence of an intergranular glass phase.
- Intergranular glass phase was present when pre-spun hydrolysis of silica was not accomplished.
- Commercial mullite fibers showed the presence of intergranular glass phase.
- Grain growth was not significant for temperatures up to 1400°C.
- Grain growth was not significant for periods as long as 12 hours at 1200°C.

Future Work

Although extensive research has been conducted on the processing of mullite fibers, additional research is proposed in several areas. These include:

- Evaluate different techniques to inhibit grain growth in mullite fibers.
- Investigate the possibility of using the microwave energy in processing of mullite fibers. The study might include:
 - measure the dielectric properties of fibers at different temperatures;
 - design microwave ovens for the different processing stages (i.e., organic removal, dehydroxide and sintering).

- study the change in reaction kinetics compared to conventional heating, and
- examine the effect of microwave on drying and organoleptic, browning, malting transformation, and grain growth.

REFERENCES

Agarwal, B. D. Agarwal and L. J. Bruckman, *Analysis and Fundamentals of Fiber Composites*, John Wiley & Sons, Inc., New York, NY (1989)

Amit, I. A. Amit, D. M. Dabhol, and M. Berkman, *J. Am. Ceram. Soc.*, **74**(10), 2303-2306 (1991)

Baldwin, C. P. Baldwin and A. J. Pinnell, *Solid-Gel Route for Materials Synthesis*, "Chemistry of Advanced Materials", edited by C. N. R. Rao, Blackwell Scientific Publications, Oxford, UK, pp. 1-17 (1992).

Baskaran, J. M. Baskaran, R. Jones and H. O. Hobbins, *J. of Mat. Sci. Lett.*, **5**, 714-715 (1986)

Baskaran, D. C. Baskaran, R. C. Matsuura, and D. P. Gaur, *Mater. Alloys*, Academic Press, Inc., New York, NY (1978)

Baskaran, C. J. Baskaran and G. W. Scherer, *Solid-Gel Process: The Physics and Chemistry of Solid-Gel Processing*, Academic Press, Inc., San Diego, CA (1990)

Chaitin, R. R. Chaitin, *Computing, Materials, Science, and Technology*, Springer-Verlag New York Inc., New York, NY (1987)

Heidrich, W. D. Heidrich, A.R. Chaudhuri and W.C. Miller, *U.S. Patent*, 4,335,412 (1982)

Holm, W.G. Holmstrom, S.L. Hinrichs, P. Newmann, N.R. Denk, P.M. Smith and C.J. Baskaran, *J. Am. Ceram. Soc.*, **73**(10), 2363-2367 (1990)

Hoover, G. Hoover, *Am. Ceram. Soc. Bull.*, **70**(2), 212-216 (1993)

Huang, M. L. Huang, *Industrial Spectroscopy in Surface Chemistry*, Marcel Dekker, Inc., New York, NY (1987)

Huang, T. Huang, F. Kusner and B. Matsuura, *J. Non-Crys. Solids*, **108**, 18-22 (1989)

Han00 L.L. Hsieh and J.K. Wei, *Chem. Rev.*, **100**, 135-73 (2000).

Herr77 P. C. Hergen, *Principles of Colloid and Surface Chemistry*, Merrill Dekker, Inc., New York, NY (1977).

Hori91 S. Horie, K. Taya, Y. Abe, A. Poins, R. Kato, *J.M. Paris*, **49**, 193-213 (1991).

Hull71 D. Hull, *An Introduction to Composite Materials*, Cambridge University Press, Cambridge, UK (1971).

Hull90 J.C. Hull and G.L. Moody, *J. Am. Ceram. Soc.*, **73**(4), 173-76 (1990).

Hull91 J.C. Hull and G.L. Moody, *J. Non-Cryst. Solids*, **14**, 1-9 (1991).

Ind79 R. K. Iler, *The Chemistry of High Polymers, Preparation, Colloid and Surface Reactions, and Biochemistry*, John Wiley & Sons, Inc., New York, NY (1979).

Jain97 M.G.M. Jainal, Z. Nafisi and S. Sastri, *J. Am. Ceram. Soc.*, **80**(3), C7-C9 (1997).

Jain98 M.G.M. Jainal, H. Arai, Z. Nafisi and T. Akiba, *J. Am. Ceram. Soc.*, **81**(4), 2296-2309 (1998).

Jain98 Z.D. Jamborska, *The Structure and Properties of Engineering Materials*, John Wiley & Sons, Inc., New York, NY (1998).

Joh87 D.D. Johnson, A.R. Holt and M.F. Greber, *Ceram. Eng. Sci. Proc.*, **8**(14), 244-254 (1987).

Jow98 R. W. Jow, *Fundamental Principles of Solid-State Technology*, The Institute of Metals, London, UK (1998).

Kan77 K.A. Kan, H.G. Sisson, *J.M. Paris*, #1947,601 (1977).

Kan93 G-D Kan, D-A Lee, H-I Lee, and S-J Kim, *Int. J. Sol. and Eng.*, **A10**, 171-176 (1993).

Kang55 W.D. Kingery and M. Wan, *J. Appl. Phys.*, **26**(10), 1207-1212 (1955).

Kang79 W. D. Kingery, H. K. Bowen, and D. R. Uhlmann, *Introduction to Ceramics*, John Wiley & Sons, Inc., New York, NY (1979).

Kwiatkowski, G.C. *Kwiatkowski, L. Am. Phys.* 26, 1050-1103 (1947).

Levy, G. Lewinsohn, C. Antes and A.R. Bennett. *Composite Science and Technology*, II, 67-76 (1990).

Li, D.X. and W.J. Thomson. *L. Mater. Res.* 27, 1923-1939 (1992).

Li, D.X. and W.J. Thomson. *L. Am. Ceram. Soc.* 73(9), 394-397 (1990).

Li, D.X. and W.J. Thomson. *L. Am. Ceram. Soc.* 73(9), 574-578 (1990).

Li, D.X. and W.J. Thomson. *L. Am. Ceram. Soc.* 73(9), 1983-1987 (1990).

Malone, J.D. *Malone, L. Solid-State Solids*, 8, 1-18 (1982).

Mallik, P.K. *Fiber Reinforced Composites, Materials, Manufacturing, and Design*. Marcel Dekker, Inc., New York, NY (1988).

Miles, T.J. Miles, R. and J.W. Langford. *L. Am. Ceram. Soc.* 73(9), 398-400 (1990).

Nakagawa, K. *Nakagawa, U.S. Patent*, #4,364,946 (1982).

Napper, D. H. *Napper, Binks, and al. Colloidal Dispersion*. Academic Press, Inc., London, UK, pp. 12-14 (1989).

Overby, J. T. G. Overby and H. G. Bergendy "De Jong-Soh of Microenclosed Colloids with Encapsulated Plasma," in *Colloid Systems*, edited by H. R. Krey, Elsevier Publishing Company, Inc., New York, NY, p. 129 (1987).

Park, J.A. Park, X.W. Zhang, A.P. Tonos and B.E. Yoldas. *L. Am. Ceram. Soc.* 73(9), 198-207 (1990).

Perry, M. R. *Perry, Leach-Babcock Fiber Composites*. Prentice-Hall Inc., Elmsford, NY (1986).

Prestwich, S. Prestwich and P.J. King. *L. Am. Ceram. Soc.* 73(9), 191-193 (1990).

Royl, J. S. *Royl, Introduction to the Principles of Ceramic Processing*. John Wiley & Sons, Inc., New York, NY (1988).

Richter, R.A. Richter, C.J. Goodwin and H.C. Stevens, *J. Am. Chem. Soc.*, **73**(14), 3404-3409 (1951).

Reed79 M.D. Reed, R.B. Langford, S.T. Tsu, and J.A. Paul, *Adv. Colloid. Sci. Biol.*, **20**(7), 691-697 (1979).

Reed82 M.D. Reed and J.A. Paul, *J. Am. Chem. Soc.*, **85**(1), 69-77 (1982).

Reed87 M.D. Reed and B.-Y. Chen, *J. Non-Crys. Solids*, **82**, 343-356 (1987).

Sanchez Sanchez, J. Llorente, M. Henry and F. Balmerouze, *J. Non-Crys. Solids*, **108**, 45-55 (1989).

Schmid H. Schmid, L. Moaveni and A. Schmid, *J. of Non. So.*, **21**, 405-412 (1982).

Schmidt B. Schmidt, *Adv. Colloid. Mat.*, **20**(1), 263-297 (1980).

Sequoia H.C. Stevens and B.D. Johnson, *Chemical Engineering and Science Proceedings*, The American Ceramic Society, Inc., Columbus OH, p. 1231-1239 (1985).

Sequoia H.C. Stevens, *Adv. Colloid. Sci. Biol.*, **62**(17), 1371-1396 (1992).

Sparks J.S. Sparks and G.S. Walker, *Adv. Colloid. Mat.*, **39**(1), 309-319 (1989).

Stevens S. Stevens and J.A. Henry, *J. Am. Chem. Soc.*, **73**(14), 3409-3416 (1951).

Stevens K. Saito, T. Matsuyama, S. Saito and T. Sogaawa, *J. Non-Crys. Solids*, **79**, 165-176 (1986).

Stevens T.B. Stevens, U.S. Patent, #4,377,369 (1983).

Tiwari V.K. Tiwari, *Mechanics of Fiber Composites*, Wiley Eastern Limited, New Delhi, India (1979).

Tucker D.J. Tucker, J.S. Sparks and D.C. Baker, *Adv. Colloid. Sci. Biol.*, **62**(17), 1371-1396 (1992).

Tucker C.W. Tucker, *Adv. Colloid. Sci. Biol.*, **20**(1), 1487-1499 (1980).

Van Krevel L. H. Van Krevel, *Physical Chemistry for Engineers*, John Wiley Publishing Company Inc., Reading, MA (1964).

Verma, K.R. Venkatesan, L.T. Moeni, M.D. Sankar and J.H. Sauerwein, *Chem. Eng. Sci. Proc.*, 129-130, 1911-1918 (1992).

Wardle, W.C. Wu and J. W. Hallock, *J. Am. Chem. Soc.*, 74(1), 165-172 (1952).

Wardle, W.C. Wu and J. W. Hallock, *J. Am. Chem. Soc.*, 77(1), 393-397 (1955).

Wardle, H. B. Wark, *Encyclopedic Colloid Chemistry*, John Wiley & Sons, Inc., New York, NY (1930).

Wardle, H. B. Wark, *Colloid Chemistry*, John Wiley & Sons, Inc., New York, NY (1949).

Yates, B.E. Yolton and D.P. Purdon, *J. Mat. Sci.*, 23, 1993-1999 (1993).

Zarikis, J. Zarikis, *Glasses and the Human Eye*, Cambridge University Press, Cambridge, U.K. (1992).

Biographical Sketch

Suhwan Al-Aasifi was born in Baghdad on November 14, 1965. He was raised in Hay Al-Addi on the western side of Baghdad. In 1983 he was admitted to the University of Mosul and majored in mechanical engineering. In 1984 he transferred to the University of Baghdad where he continued his studies in mechanical engineering. In 1988 Suhwan was selected to continue his education in the Department of Nuclear Engineering. He completed his undergraduate studies in 1991, receiving a Bachelor of Science degree in nuclear engineering. In 1994 he was awarded a government scholarship to continue his graduate education in the United States. He was admitted to the University of Florida in May of 1994 where he joined Dr. Clark's graduate research group. His research focused on the microstructural joining of alumina ceramic with alumina glass and he was awarded his Master of Science degree in May, 1995. Suhwan joined Dr. Bissner's research group in 1995 where his studies focused on processing of continuous alumina fibers prepared using sol-gel techniques. He is a member of the American Ceramic Society, the National Institute of Ceramic Engineers and Ceramic, the ceramic engineering honor society. His hobbies include snookerball, tennis, bowling and travel.

I certify that I have read this study and that in my opinion it conforms to acceptable standards of scholarly presentation and is fully adequate, in scope and quality as a dissertation for the degree of Doctor of Philosophy.



Joseph M. Saramat
Professor of Materials
Science and Engineering

I certify that I have read this study and that in my opinion it conforms to acceptable standards of scholarly presentation and is fully adequate, in scope and quality as a dissertation for the degree of Doctor of Philosophy.



Larry L. Heath
Graduate Research Professor of
Materials Science and Engineering

I certify that I have read this study and that in my opinion it conforms to acceptable standards of scholarly presentation and is fully adequate, in scope and quality as a dissertation for the degree of Doctor of Philosophy.



E. Don Wherry
Professor of Materials
Science and Engineering

I certify that I have read this study and that in my opinion it conforms to acceptable standards of scholarly presentation and is fully adequate, in scope and quality as a dissertation for the degree of Doctor of Philosophy.



Anthony B. Truscan
Associate Professor of Materials
Science and Engineering

I certify that I have read this study and that in my opinion it conforms to acceptable standards of scholarly presentation and is fully adequate, in scope and quality as a dissertation for the degree of Doctor of Philosophy.



Marvin V. Sander

Associate Professor of Aerospace
Engineering, Mechanics, and Engineering
Sciences

This dissertation was submitted to the Graduate Faculty of the College of
Engineering and to the Graduate School and was accepted as partial fulfillment of
the requirements for the degree of Doctor of Philosophy.

December 1994



Walter M. Phillips
Dean, College of Engineering

Karen A. McFerran
Dean, Graduate School